12th AIAA/CEAS Aeroacoustics Conference (27th AIAA Aeroacoustics Conference), 8–10 May 2006, Boston

Surface-Waves, Stability, and Scattering for a Lined Duct with Flow

E.J. Brambley*, N. Peake†

University of Cambridge, Cambridge CB3 0WA, UK

We consider a straight cylindrical duct with a steady subsonic axial flow and a reacting boundary (e.g. an acoustic lining). The wave modes are separated into ordinary acoustic duct modes, and surface modes confined to a small neighbourhood of the boundary. Many researchers have used a mass–spring–damper boundary model, for which one surface mode has previously been identified as a convective instability; however, we show the stability analysis used in such cases to be questionable. We investigate instead the stability of the surface modes using the Briggs–Bers criterion for a Flügge thin-shell boundary model. For modest frequencies and wavenumbers the thin-shell has an impedance which is effectively that of a mass–spring–damper, although for the large wavenumbers needed for the stability analysis the thin-shell and mass–spring–damper impedances diverge, owing to the thin shell's bending stiffness. The thin shell model may therefore be viewed as a regularization of the mass–spring–damper model which accounts for nonlocally-reacting effects. We find all modes to be stable for realistic thin-shell parameters, while absolute instabilities are demonstrated for extremely thin boundary thicknesses. The limit of vanishing bending stiffness is found to be a singular limit, yielding absolute instabilities of arbitrarily large temporal growth rate. We propose that the problems with previous stability analyses are due to the neglect of something akin to bending stiffness in the boundary model. Our conclusion is that the surface mode previously identified as a convective instability may well be stable in reality.

Finally, inspired by Rienstra's recent analysis, we investigate the scattering of an acoustic mode as it encounters a sudden change from a hard-wall to a thin-shell boundary, using a Wiener–Hopf technique. The thin-shell is considered to be clamped to the hard-wall. The acoustic mode is found to scatter into transmitted and reflected acoustic modes, and surface modes strongly linked to the solid waves in the boundary, although no longitudinal or transverse waves within the boundary are excited. Examples are provided that demonstrate total transmission, total reflection, and a combination of the two. This thin-shell scattering problem is preferable to the mass–spring–damper scattering problem presented by Rienstra, since the thin-shell problem is fully determined and does not need to appeal to a Kutta-like condition or the inclusion of an instability in order to avoid a surface-streamline cusp at the boundary change.

I. Introduction

Acoustic waves in a straight cylindrical hard-wall duct are well understood, with the familiar solution in terms of Bessel's functions of the first kind. If a uniform axial mean flow is introduced, the only additional effect is to produce a Doppler shift to the frequency. If the duct boundary is deformable and allowed to react to the acoustic perturbations (for example, a vortex sheet boundary layer over a Helmholtz resonator acoustic lining), the majority of duct modes have their wavenumbers shifted slightly from their hard-wall values. However, Rienstra recently noted[1] that modes of another type are present with a deformable boundary that have no hard wall equivalent. These modes tend to be confined to within a small neighbourhood of

*PhD student, DAMTP, University of Cambridge, Wilberforce Rd. Cambridge CB3 0WA, UK. AIAA Member.

†Professor of Applied Mathematics, DAMTP, University of Cambridge, Wilberforce Rd. Cambridge CB3 0WA, UK. AIAA member.

the boundary, and consequently are termed *surface modes*. To distinguish them, the modes with hard wall equivalents are termed *acoustic modes*. The effect of mean flow on these surface modes is significant, and indeed they are qualitatively different depending on whether mean flow is present or not. The surface modes, being tightly coupled with the boundary, also have deep connections with the stability of the boundary (or, in the example of a vortex sheet over an acoustic lining, the stability of the vortex sheet).

The behaviour of the boundary is characterized by its impedance, $Z(k, m, \omega)$. The impedance is defined as $Z = p/v$, where a harmonic forcing $p \exp\{\mathrm{i}\omega t - \mathrm{i}kx - \mathrm{i}m\theta\}$ produces a corresponding boundary velocity $v \exp\{\cdots\}$. For example, a commonly used simple boundary model is that of a mass–spring–damper (effectively a modified Winkler foundation), for which the radial boundary displacement w is given by

$$d\frac{\partial^2 w}{\partial t^2} + R\frac{\partial w}{\partial t} + bw = p \qquad \Rightarrow \qquad Z = R + \mathrm{i}d\omega - \mathrm{i}b/\omega \tag{1}$$

where d, b, and R are positive real constants representing the mass, spring, and damping terms respectively. The absence of k and m in Z above is because the mass–spring–damper boundary is locally reacting.

Rienstra[1] went on to show that, in an incompressible limit and for a mass–spring–damper boundary, one surface mode might be interpreted as an instability. Weight was added to this argument by Rienstra & Peake,[2] who considered the acoustic scattering from a sudden boundary change, and found that the surface streamline had an $O(x^{1/2})$ cusp if no instability was present, while this could be made to be a more favourable $O(x^{3/2})$ if an instability was included and an appropriate Kutta-like condition satisfied.

There are many criteria for analysing the stability of a linear system, the most common being that of Briggs & Bers.[3,4] However, as was pointed out by Rienstra & Peake,[2] owing to a technicality the Briggs–Bers criterion cannot be applied to a mass–spring–damper boundary model, since $\mathrm{Im}(\omega(k))$ is not bounded below for real k. In other words, for arbitrary initial conditions the temporal growth rate is unbounded. This is a well-known problem, the most common example of which is the widely-studied Kelvin–Helmholtz vortex sheet instability. For example, Jones & Morgan analysed the stability of a vortex sheet subject to an acoustic line source,[5,6] and found an unbounded temporal growth rate that caused problems with imposing causality. Crighton & Leppington also considered the scattering of an acoustic line source by a vortex sheet,[7] this time being shed from a semi-infinite plate, and discovered that by taking the time-harmonic solution with ω purely imaginary and analytically continuing the solution to real ω, a desirable but unproved Kutta condition was satisfied at the trailing edge of the plate. Both Jones & Morgan and Crighton & Leppington concluded by explicitly constructing a causal Green function, which in both cases was highly singular and expressed in terms of ultradistributions. The question of stability for a vortex sheet was finally resolved by Jones,[8] by regularising the vortex sheet by considering a shear layer of finite thickness h. Jones concluded that for h small but nonzero an instability was present that could be represented in terms of conventional functions, and which in the limit $h \to 0$ yielded the previous ultra-distribution result.

An alternative stability criterion[9] has recently found popularity,[1,2,10,11] which some authors have termed the"Crighton–Leppington" criterion. It involves assuming that all modes decay in space for ω purely imaginary, and therefore that the stability of the modes may be deduced by analytic continuity in ω with $|\omega|$ fixed and $\arg(\omega)$ running from $-\pi/2$ to 0. Unfortunately, this method is not universally valid, and in particular examples are provided in appendix A for which this method fails.

We begin in section II by setting out the mathematical model used throughout the paper, and then deriving the dispersion relation for this model. We then consider the behaviour of the surface modes in section III, and demonstrate the unbounded temporal growth rate for a mass–spring–damper boundary model mentioned by Rienstra & Peake.[2] This leads us to reconsider the boundary model, and in section IV the impedance is derived for a thin cylindrical shell, the outside of which is sprung and damped (as if by a modified Winkler foundation). The surface modes are characterized for this boundary model, and the limit of zero shell thickness is shown to correspond to the mass–spring–damper boundary model. We then turn to the question of stability for a thin-shell boundary model in section V, and the temporal growth rate is shown to be bounded. The thin-shell thickness therefore regularizes the mass–spring–damper boundary model and enables the Briggs–Bers criterion to be applied. We find the thin shell to be either stable or to admit absolute instabilities, and the values of the mean-flow Mach number and thin-shell thickness needed to induce these absolute instabilities are investigated. Finally, in section VI we reconsider the scattering problem of Rienstra & Peake, and show that the thin-shell boundary model leads to an even more favourable $O(x^2)$ surface streamline without necessarily needing an instability to be present. We compute examples demonstrating scattering, complete transmission, and complete reflection, for different thin shell parameters.

II. Governing equations

We consider the steady flow of a compressible inviscid fluid within a straight cylindrical duct of radius r_0. The fluid has constant entropy, constant density ρ_0, constant sound speed c_0, and the flow is in the axial x direction with constant subsonic speed U. To this steady flow, we consider the evolution of small time-harmonic perturbations (e.g. sound) which are sufficiently small that we may linearize and ignore all quadratic and higher terms.

In order to make apparent the important scalings, and to simplify the notation, all quantities are nondimensionalized. Distances are nondimensionalized by r_0, speeds by c_0, densities by ρ_0, times by c_0/r_0, and pressures by $\rho_0 {c_0}^2$. With this nondimensionalization, the axial flow speed U is equal to the Mach number.

Goldstein[12] showed that a small perturbation may be decomposed into entropic, vortical, and acoustic parts, and gave equations for their evolution. Here, we are only interested in the acoustic perturbations, for which the evolution of the linearized pressure, density, and velocity (p, ρ, and $\boldsymbol{u}$) is given in terms of the velocity potential ϕ, as

$$\frac{\mathrm{D}^2\phi}{\mathrm{D}t^2} - \nabla^2\phi = 0, \qquad p = \rho = -\frac{\mathrm{D}\phi}{\mathrm{D}t}, \qquad \boldsymbol{u} = \boldsymbol{\nabla}\phi, \tag{2}$$

where $\mathrm{D}/\mathrm{D}t = \partial/\partial t + U\partial/\partial x$. By separation of variables, this has solutions

$$\phi = A\mathrm{J}_m(\alpha r)\exp\{\mathrm{i}\omega t - \mathrm{i}kx - \mathrm{i}m\theta\}, \qquad \alpha^2 = (\omega - Uk)^2 - k^2,$$

where A is an arbitrary constant amplitude. The frequency ω, using the nondimensionalization above, is equal to the Helmholtz number, also known as the "ka" value.

The allowable values of α are given by the boundary conditions. We model the duct boundary as a flexible impermeable surface (for example, a thin vortex sheet boundary layer over an acoustic lining, as considered by Rienstra[1]), with impedance $Z(k, \omega, m)$. The motion of the boundary complicates the no-flux boundary condition $\boldsymbol{u}\cdot\hat{\boldsymbol{n}} = 0$ applied on the surface, since both the position of the surface and the direction of the surface normal $\hat{\boldsymbol{n}}$ are unsteady and dependent on the flow. For a general geometry and impedance, Myers[13] derived the linearized no-flux boundary condition to be

$$\mathrm{i}\omega\boldsymbol{u}\cdot\boldsymbol{n} = (\mathrm{i}\omega + \boldsymbol{U}\cdot\boldsymbol{\nabla} - (\boldsymbol{n}\cdot\boldsymbol{\nabla}\boldsymbol{U})\cdot\boldsymbol{n})\,p/Z, \tag{3}$$

where $\boldsymbol{n}$ is the unperturbed surface normal out of the fluid, $\boldsymbol{U}$ is the steady mean flow, $\boldsymbol{u}$ and p are the linearized velocity and pressure, and all quantities are evaluated on the unperturbed boundary. For our problem, substituting the solution for ϕ into this boundary condition yields the dispersion relation

$$1 - \frac{(\omega - Uk)^2}{\mathrm{i}\omega Z}\frac{\mathrm{J}_m(\alpha)}{\alpha\mathrm{J}'_m(\alpha)} = 0. \tag{4}$$

Note that since $\mathrm{J}_m(-r) = (-1)^m\mathrm{J}_m(r)$, it does not matter which branch is chosen for α. The hard-wall dispersion relation $\mathrm{J}'_m(\alpha) = 0$ is recovered by taking $Z \to \infty$.

III. Surface modes

Figure 1 shows the solutions to the dispersion relation (4) for the axial wavenumber k. The close correspondence between the hard-wall modes and the impedance-boundary acoustic modes is clear in figure 1(a), although the impedance boundary includes some damping which modifies the cuton–cutoff behaviour of the impedance-boundary acoustic modes. Figure 1(b) shows two series of surface modes (each series with one mode per azimuthal order m), for which there are no hard-wall equivalents. The surface modes for $m \lesssim \omega$ are as predicted by Rienstra.[1] However, for $m \gtrsim \omega$ one surface mode series occurs in a different region of the k plane than predicted by Rienstra, and therefore might be interpreted on first glance as left propagating, whereas for $m \lesssim \omega$ it is interpreted as right propagating. Rienstra's predictions were derived in the limit $\omega \to \infty$ with m fixed, and Rienstra noted that these predictions might break down if m were comparable with ω.

As an aeroengine application, consider a fan with m blades, rotating at the nondimensionalized angular velocity Ω. The blade passing frequency (BPF) is therefore $\omega = \Omega m$. With the nondimensionalization used here, Ω is equal to the blade-tip Mach number, and is therefore about 1 or less (for a typical aeroengine,[14] at

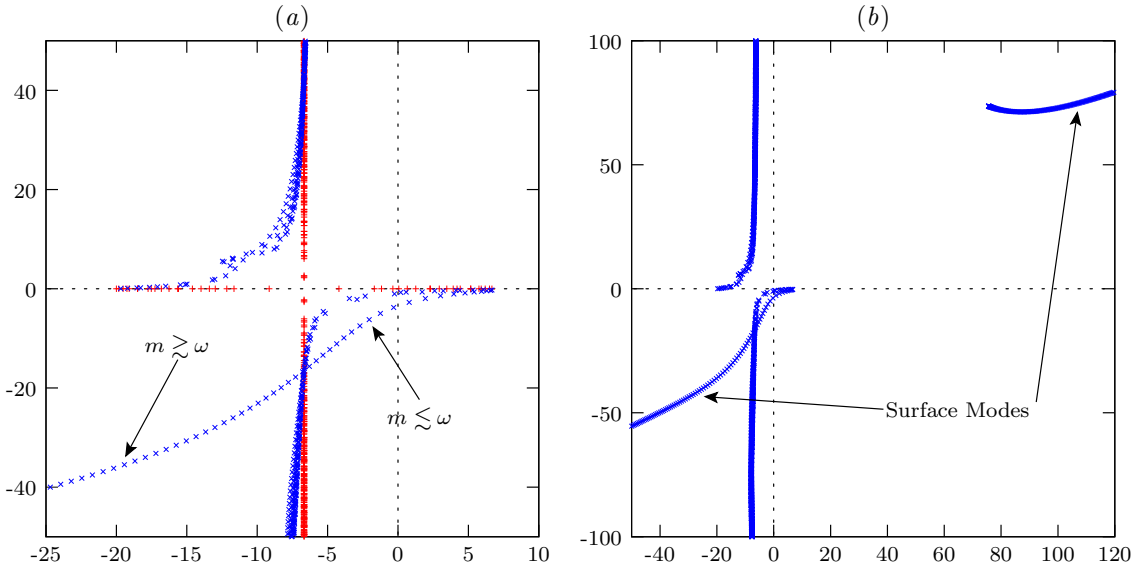

Figure 1. Axial wavenumbers k, for $U = 0.5$, $\omega = 10$. (*a*) Comparison between hard-wall wavenumbers (+) and impedance boundary with $Z = 2 - \mathrm{i}$ (×). (*b*) Larger view showing two surface mode series, for $Z = 2 - \mathrm{i}$.

sideline $\Omega \approx 1.29$, at cutback $\Omega \approx 1.11$, while at idle $\Omega \approx 0.75$). For aeroengine applications, therefore, the assumption that $\omega \gg m$ is not appropriate. Rienstra's predictions were recently generalized by Brambley & Peake[15] to relax this assumption. The generalized surface-mode dispersion relation, written in terms of k and m, is

$$\mu - \frac{(\omega - Uk)^2}{\mathrm{i}\omega Z} = 0, \qquad \text{where} \qquad \mu = \sqrt{k^2 + m^2 - (\omega - Uk)^2} \qquad \text{and} \qquad \mathrm{Re}(\mu) > 0. \tag{5}$$

Modes satisfying this dispersion relation, but with $\mathrm{Re}(\mu) < 0$, are here termed *fake surface modes*. The line $\mathrm{Re}(\mu) = 0$ is an anti-Stokes line. It corresponds to the surface modes becoming acoustic modes, no longer being localized about the duct boundary, and hence the asymptotics used to derive (5) breaking down.

A. Unbounded temporal growth rate for a locally-reacting boundary

For the mass–spring–damper boundary model, $\mathrm{Im}(\omega(k))$ is not bounded below for real k, and so the Briggs–Bers stability criterion is not applicable.[2] To see this, substitute the mass–spring–damper impedance (1) into the asymptotic dispersion relation (5) to find, in the limit $|k| \to \infty$, to leading order

$$\omega \sim -\mathrm{i}\left(\frac{U^2}{d\beta}k\right)^{1/2}, \tag{6}$$

where $\beta^2 = 1 - U^2$. This behaviour is also seen for the simple $\cot(\omega L)$ Helmholtz resonator boundary model. Figure 2 demonstrates this unbounded growth rate, by plotting the image of the real k axis into the ω-plane for the full dispersion relation (4).

Because of this unbounded behaviour, the Briggs–Bers stability analysis is inapplicable. Consequently, a method suggested by Rienstra[9] has previously been used[1, 2, 10] to analyse the stability of the mass–spring–damper boundary. Unfortunately, this method is not universally valid; for example, appendix A gives an example for which Rienstra's method fails. In addition, Rienstra's method does not consider the possibility of absolute instability, as demonstrated by the second example in appendix A. Here, we consider regularising the problem, as shown in figure 2, by including a bending stiffness in our boundary model. This is similar to Jones' regularization of the vortex sheet problem by considering a finite-thickness shear layer.[8] The bending stiffness is negligible provided k is small, but for large k it becomes significant and bounds $\mathrm{Im}(\omega(k))$ below. We now consider this new boundary model in detail.

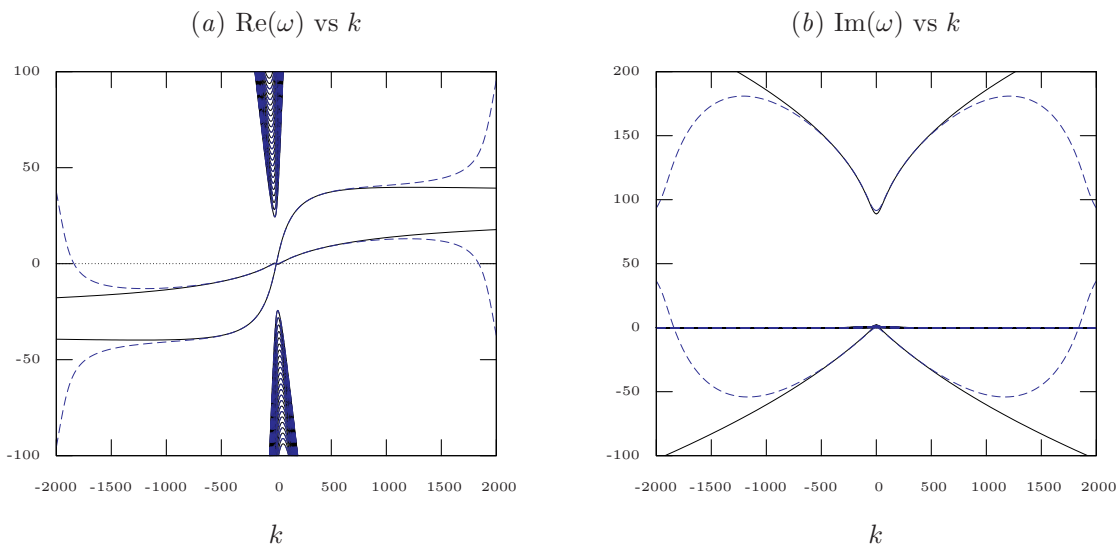

Figure 2. Trajectories of $\omega(k)$ for k real. Solid lines correspond to the mass–spring–damper boundary model. The dashed lines show the effect of adding a small bending stiffness in the boundary model. $U = 0.5$, $m = 24$, $b = 6.5$, $d = 0.022$, **and** $R = 3$.

IV. The Flügge thin-shell boundary model

We consider the duct boundary to be a thin cylindrical shell, as shown in figure 3. The Flügge thin-shell equations of motion are used here, as given by Païdoussis.[16] As well as the radial displacement w, the thin-shell boundary has an axial displacement u and an azimuthal displacement v, as shown in figure 3. The outside of the thin shell is subjected to a spring and damping force (i.e. a modified Winkler foundation), so that the total outward force per unit area on the thin shell is $p^* = p - bw - R\partial w/\partial t$, where p is the linearized acoustic fluid pressure at the boundary, and b and R are the spring and damping strengths respectively. The thin-shell equations are simplified slightly by assuming that the thin-shell thickness $h \ll 1$, and that $2m^2 - 1 \ll (k^2 + m^2)^2$. This gives the thin-shell impedance as

$$Z = R - \mathrm{i}\left({c_l}^2 d + b\right)/\omega + \mathrm{i}d\omega - \frac{\mathrm{i}{c_l}^2 d}{\omega}\left(\frac{h^2}{12}\left(k^2 + m^2\right)^2 - A_1\frac{\mathrm{i}u}{w} - A_2\frac{\mathrm{i}v}{w}\right), \tag{7a}$$

where

$$\begin{pmatrix} a_{11} & a_{12} \\ a_{12} & a_{22} \end{pmatrix}\begin{pmatrix} \mathrm{i}u/w \\ \mathrm{i}v/w \end{pmatrix} = \begin{pmatrix} A_1 \\ A_2 \end{pmatrix}, \tag{7b}$$

$$\begin{aligned} a_{11} &= k^2 + \frac{1-\nu}{2}m^2 - \frac{\omega^2}{{c_l}^2}, & a_{12} &= \frac{1+\nu}{2}mk, & A_1 &= k\left[\nu + \frac{h^2}{12}\left(k^2 - \frac{1-\nu}{2}m^2\right)\right], \\ a_{22} &= m^2 + \frac{1-\nu}{2}k^2 - \frac{\omega^2}{{c_l}^2}, & & & A_2 &= m\left[1 + \frac{h^2}{12}\frac{3-\nu}{2}k^2\right], \end{aligned} \tag{7c}$$

and ${c_l}^2 = E/(\rho_s(1-\nu^2))$ is the square of the speed of longitudinal compressive waves in the boundary material, $d = \rho_s h$ is the shell mass per unit area, and the properties of the boundary material ρ_s, E and ν are the density, Young's modulus, and Poisson's ratio respectively.

If the $A_1 u/w$ and $A_2 v/w$ terms in (7a) can be neglected, a much simpler impedance is obtained:

$$Z = R - \mathrm{i}\left({c_l}^2 d + b\right)/\omega + \mathrm{i}d\omega - \mathrm{i}B\left(k^2 + m^2\right)^2/\omega, \tag{8}$$

This is effectively a mass–spring–damper impedance, with the thin shell contributing an extra ${c_l}^2 d$ spring force, together with a bending stiffness $B = {c_l}^2 d h^2/12$. One situation where the $A_1 u/w$ and $A_2 v/w$ terms

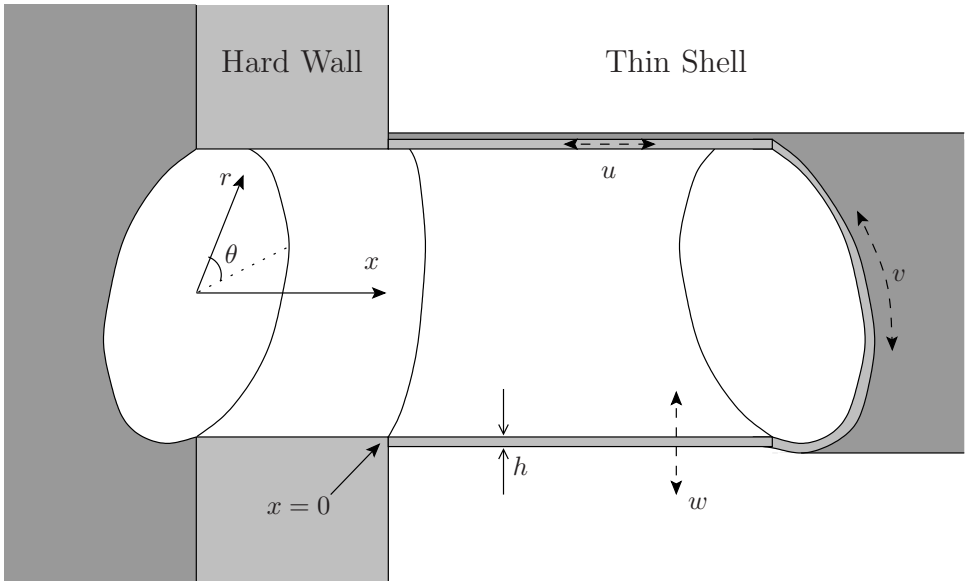

Figure 3. Schematic of a cylindrical duct with a sudden change from hard-wall boundary for $x < 0$ to thin-shell boundary for $x > 0$. The small unsteady perturbations to the position of the thin shell are given by u, v, and w.

can certainly be neglected is if k is large and $m/k \lesssim O(1)$ (of particular interest for stability analysis). Then, provided the determinant of (7b) is nonzero, it can be shown that

$$u/w = O(h^2 k), \qquad v/w \lesssim O(h^2 k), \qquad A_1 u/w + A_2 v/w = O(h^4 k^4),$$

so that the $A_1 u/w$ and $A_2 v/w$ terms are insignificant compared to the $B(k^2 + m^2)^2$ bending stiffness term.

The determinant of (7b) is zero when $k = \pm k_l$ or $k = \pm k_t$, where

$$k_l{}^2 = \omega^2/\mathrm{c}_l{}^2 - m^2 \qquad \text{and} \qquad k_t{}^2 = \omega^2/\mathrm{c}_t{}^2 - m^2 \tag{9}$$

and $\mathrm{c}_t = \mathrm{c}_l\sqrt{(1-\nu)/2}$ is the speed of transverse waves in the duct boundary. We take $\mathrm{Im}(k_l) < 0$, or $\mathrm{Im}(k_l) = 0$ and $\mathrm{Re}(k_l) > 0$, and similarly for k_t, so that these are the axial wavenumbers for right-propagating longitudinal and transverse solid waves in the thin-shell boundary. The zero determinant implies that these solid boundary waves propagate independently of the radial shell displacement w, and consequently independently of the fluid within the shell.

A. The thin-shell surface modes

Since the thin-shell boundary is not locally-reacting, as seen by the dependence of Z on k, the previous interpretations of the surface modes[1, 15] are no longer valid. The asymptotic dispersion relation (5) is still valid, however, and may be rearranged to give

$$\left(a_{11}a_{22} - a_{12}{}^2\right)^2 (\omega - Uk)^4 - \left(\left(a_{11}a_{22} - a_{12}{}^2\right) \mathrm{i}\omega Z\right)^2 \left(k^2 + m^2 - (\omega - Uk)^2\right) = 0. \tag{10}$$

This is an 18^{th} order polynomial in k for fixed ω, or a 14^{th} order polynomial in ω for fixed k. There are therefore 18 surface modes, compared with only 4 for a locally reacting boundary, although of course some of these may be fake surface modes.

Figure 4 gives an example of these surface modes. Figure 4(a) demonstrates the accuracy with which the surface modes are predicted by (10). Figure 4(b) shows, as well as can be in a two-dimensional plot, the behaviour of the surface modes in the limit $h \to 0$. Of the 18 potential surface modes, one real surface mode and one fake surface mode converge to each of k_l, k_t, $-k_l$, and $-k_t$, and surface modes of this type are here termed *quasi-solid* surface modes. It should be emphasized, however, that these surface modes are distinct from the solid boundary waves with axial wavenumbers $\pm k_l$ and $\pm k_t$; the quasi-solid modes are

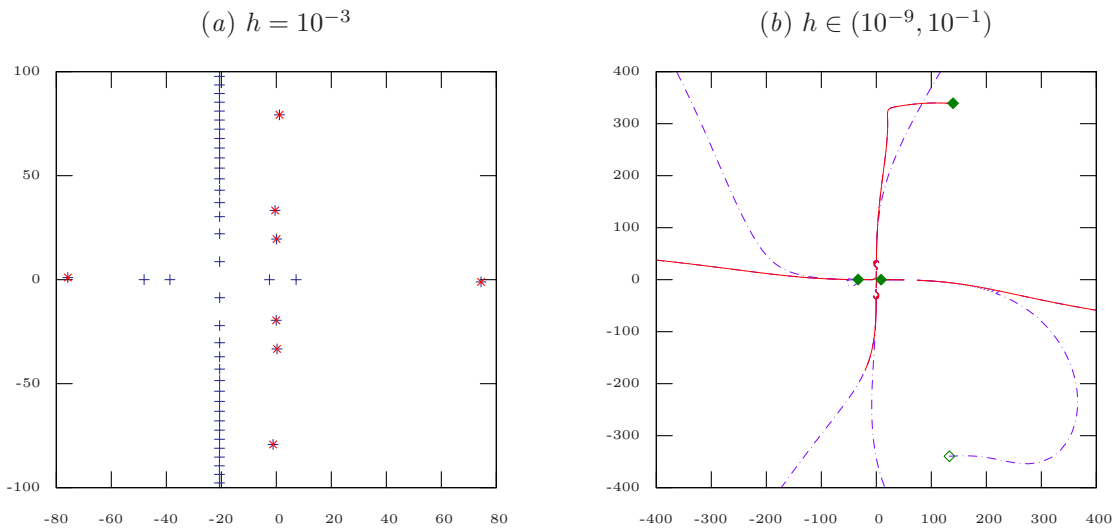

Figure 4. Surface modes in the k-plane for air within an aluminium boundary (see table 1) with external spring force $b = 1$ and damping $R = 3$, for $\omega = 31$, $U = 0.5$, and $m = 24$. (*a*) Comparison between the exact solutions (+) and solutions to (10) (×), for $h = 10^{-3}$. (*b*) Thin-shell surface modes for varying h (lines) and mass–spring–damper surface modes (diamonds). Dashed lines and hollow diamonds denote fake surface modes.

Fluid	**Solid**	$\mathbf{c_l}$	$\boldsymbol{\rho_s}$	$\boldsymbol{\nu}$
Air	Aluminium	15.8	2 200	0.33
Water	Steel	3.6	7.85	0.3

Table 1. Nondimensionalized thin-shell parameters for different materials, at standard temperature and pressure (STP).

fluid modes occurring in the vicinity of the boundary, with k close to one of $\pm k_l$ or $\pm k_t$, whereas the solid boundary waves given by $\pm k_l$ and $\pm k_t$ correspond to zeros of the determinant of (7b) and therefore produce no disturbance in the fluid at all. Of the remaining 10 surface modes, four fake and two real surface modes tend to infinity, while the other 4 surface modes tend to the mass–spring–damper values. This suggests that of the 18 potential surface modes, 8 are sustained by compressional and twisting solid mechanisms, 6 are supported by bending solid mechanisms, and four are supported by effectively mass–spring–damper mechanisms.

If the $A_1 u/w$ and $A_2 v/w$ terms may be neglected, leading to the impedance (8), then (10) may be simplified to give

$$\left(k^2 + m^2 - (\omega - Uk)^2\right)\left(\left(\mathrm{c}_l{}^2 d + b\right) + \mathrm{i}\omega R - d\omega^2 + B\left(k^2 + m^2\right)^2\right) - (\omega - Uk)^4 = 0. \tag{11}$$

This is now a polynomial of 10^{th} order in k, or of 6^{th} order in ω. This dispersion relation turns out to be remarkably accurate, even for modest values of k for which the argument for neglecting the $A_1 u/w$ and $A_2 v/w$ terms is not valid. Of course, neglecting these terms neglects the compressional and twisting components in the solid, and consequently the 8 quasi-solid surface modes that depend on these mechanisms are not modelled by (11).

V. Stability analysis

One of the reasons for considering a thin-shell boundary model is to regularize the mass–spring–damper boundary model and enable the Briggs–Bers stability criterion to be applied. For example, figure 2 shows that for air within an aluminium thin shell (with parameters as given in table 1) with thickness $h = 10^{-5}$ and an external spring force $b = 1$ and damping $R = 3$, $\mathrm{Im}(\omega(k))$ is bounded below by -100 for all real k, while for small k the results are exactly that of a mass–spring–damper with the appropriate mass, spring, and damping coefficients (as given by equation 8). We now aim to show that this is the case for all thin-shell parameters, provided $h \neq 0$, and so application of the Briggs–Bers criterion is valid in all thin-shell cases.

The behaviour of the acoustic modes for a thin-shell boundary is almost exactly the same as for a mass–spring–damper boundary, and in either case these modes are stable and similar to their hard-wall counterparts. The acoustic modes do not therefore prohibit application of the Briggs–Bers method (for the acoustic modes, in fact, $\mathrm{Im}(\omega(k))$ is bounded below by zero for real k).

The only singularities of the dispersion relation (10) are due to the zeros of the determinant of (7b), and lead to the finite values of ω given in (9). Therefore, for k in any finite real interval, $\mathrm{Im}(\omega(k))$ is bounded below. This is of course also true for a mass–spring–damper boundary. What goes wrong for the mass–spring–damper boundary is that there is a surface mode for which $\mathrm{Im}(\omega(k)) \to -\infty$ as $|k| \to \infty$, and so we now consider what happens for a thin-shell boundary's surface modes in the limit $|k| \to \infty$.

In the limit $|k| \to \infty$, we have already shown that neglecting the $A_1 u/w$ and $A_2 v/w$ terms is valid provided we are sufficiently far from a zero of the determinant of (7b). Then, using (11), we find six surface modes, for which

$$\omega = Uk \pm \sqrt{k^2 + m^2} + O\left(k^{-5}\right), \qquad \omega = \pm\sqrt{B/d}\left(k^2 + m^2 + 1/2\right) + \frac{\mathrm{i}}{2d}(R \pm 1) + O\left(k^{-1}\right),$$

as $|k| \to \infty$, where the two $\pm$ in the last equation are independent. These have the leading-order large-k behaviour of a hard-wall mode and a bending wave in an unforced cylindrical thin shell respectively; these two classifications are therefore termed *fluid* and *bending* surface modes. Although not demonstrated here, the fluid surface modes and two of the bending surface modes become the four mass–spring-damper surface modes in the limit $h \to 0$, while the other two bending surface modes tend to infinity as $h \to 0$, as mentioned previously. Accounting for zeros of the determinant of (7b) gives an additional eight surface modes, with one fake and one real surface mode for each of

$$\omega = \pm \mathrm{c}_l k + O\left(k^{-1}\right) \qquad \text{and} \qquad \omega = \pm \mathrm{c}_t k + O\left(k^{-1}\right).$$

as $|k| \to \infty$; these are the quasi-solid surface modes. Since all of the above surface modes have bounded $\mathrm{Im}(\omega(k))$ as $|k| \to \infty$, the image of the real k axis in the ω-plane has bounded imaginary part for all modes, and so the Briggs–Bers criterion is valid.

To see how the bending stiffness regularizes the mass–spring–damper problem, consider the unbounded behaviour of $\mathrm{Im}(\omega(k))$ for the mass–spring–damper boundary given in (6). With the thin-shell boundary, setting $\omega = N\sqrt{k}$ in (11) gives

$$N^2 = -\frac{U^2}{\beta d} + \frac{B}{d}k^3,$$

Thus, the mass–spring–damper behaviour is seen to hold hold provided

$$|k| \ll \left(\frac{U^2}{\beta B}\right)^{1/3}, \tag{12}$$

giving an estimate of the magnitude of k for which bending stiffness becomes important for stability. For the parameters used for figure 2, this magnitude is $|k| \approx 1850$, which agrees well with the results shown.

A. A stable example

Figure 5 shows the real k axis mapped into the ω-plane for an air-filled aluminium duct. The duct may be thought of as having a 1m radius and a shell thickness of 1mm. The many near-parallel trajectories in figure 5(a) correspond to the acoustic modes, while the few other modes are the surface modes (a fluid, a bending, and two quasi-solid modes are shown). Note that no modes are present with $\mathrm{Im}(\omega) < 0$, so that

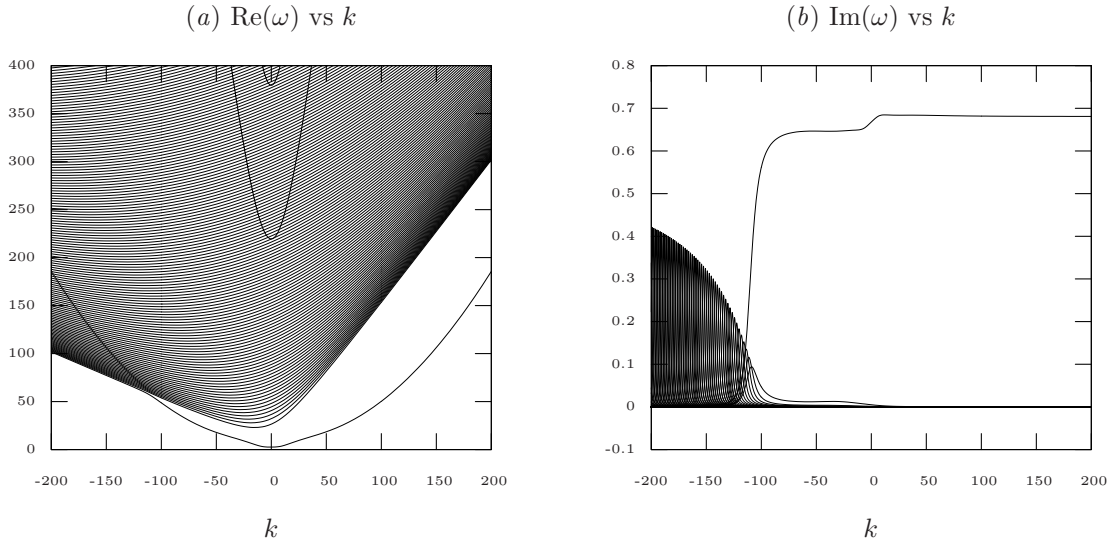

Figure 5. Trajectories of $\omega(k)$ for k real. For clarity, only modes with $\mathrm{Re}(\omega) > 0$ are shown; the behaviour for $\mathrm{Re}(\omega) < 0$ may be inferred from $-\omega^*(-k^*) = \omega(k)$, where * denotes complex conjugation. The fluid is air and the boundary is aluminium (see table 1) with $R = 3$ and $b = 1$, for $h = 10^{-3}$, $U = 0.5$, and $m = 24$.

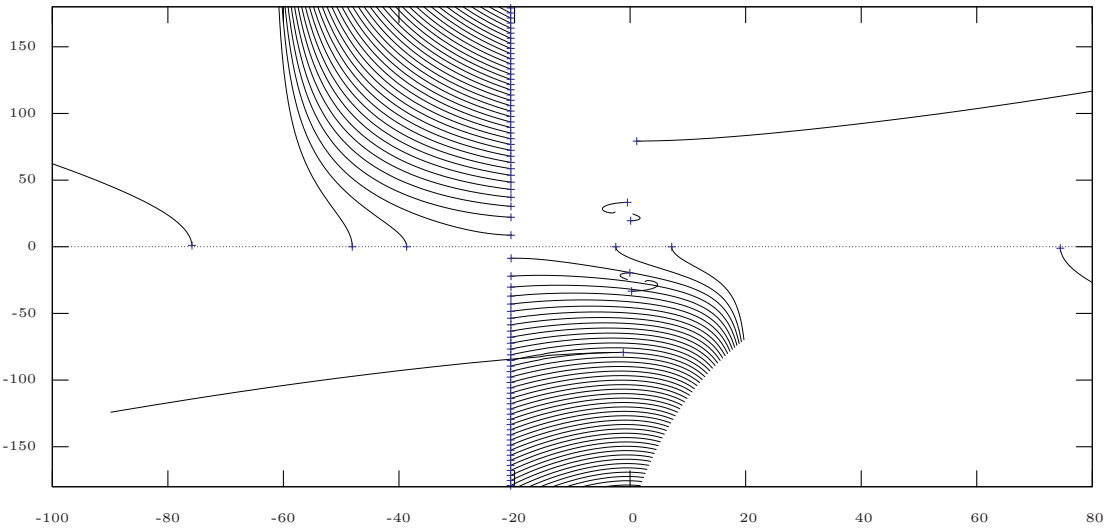

Figure 6. Trajectories of modes in the k-plane for $-100 \leq \mathrm{Im}(\omega) \leq 0$ with $\mathrm{Re}(\omega) = 31$, with crosses at $\mathrm{Im}(\omega) = 0$. As for figure 5, the fluid is air and the boundary is aluminium (see table 1) with $R = 3$ and $b = 1$, for $h = 10^{-3}$, $U = 0.5$, and $m = 24$.

the Briggs–Bers temporal inversion contour $\mathcal{C}_\omega$ may be taken arbitrarily close to the real ω axis. Hence, any mode with complex $k(\omega)$ corresponds to an exponentially-decaying mode, while if $k(\omega)$ is real, the mode is left propagating if $\mathrm{Re}(\mathrm{c}_g) < 0$, and right propagating if $\mathrm{Re}(\mathrm{c}_g) > 0$, where $\mathrm{c}_g = \partial\omega/\partial k$ is the group velocity, and there is no possibility of absolute instability. This is exactly as might have been naively expected without a detailed stability analysis, and shows that for these parameters the system is stable.

As an example of the typical Briggs–Bers treatment given in the literature, figure 6 shows the trajectories of modes in the k-plane as $\mathrm{Im}(\omega)$ is varied with $\mathrm{Re}(\omega)$ fixed, for parameters typical of the BPF mode in an aeroengine.[14] No modes cross the real k axis, and thus all modes are seen to be either exponentially decaying or propagating in the direction of the group velocity, as predicted. It should be emphasized that just this analytic continuation does not guarantee the stability of the system, without first having ascertained that $\mathrm{Im}(\omega(k))$ is bounded below for real k, and having checked that no absolute instabilities are present.

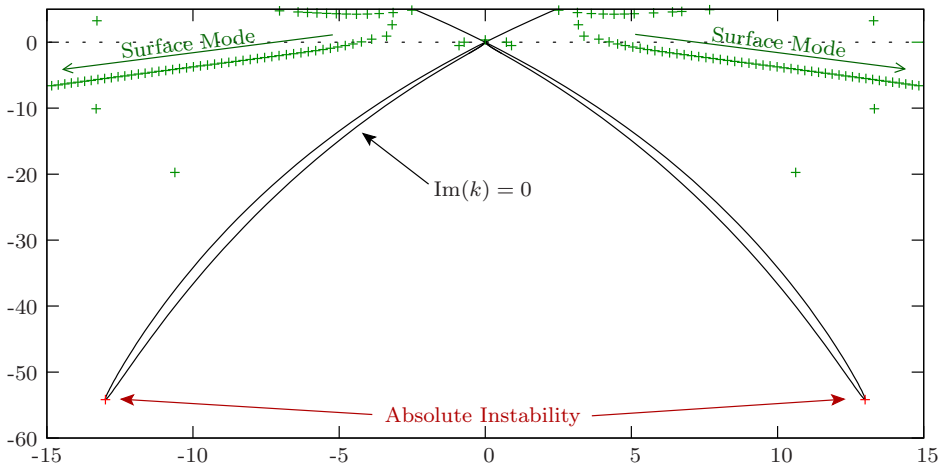

Figure 7. Values of ω for which double roots of the dispersion relation occur for some value of k. The double roots labelled "Surface Mode" are caused by one surface mode converging with successive acoustic duct modes (as shown in figure 8*a*), and the arrows point in the direction of increasing $|\mathrm{Im}(k)|$ for the double root. Parameters are for air in aluminium (see table 1), with $b = 1$, $R = 3$, $h = 10^{-5}$, $U = 0.5$, and $m = 24$ (as for the dashed line in figure 2).

B. Absolute instabilities

If, instead, we consider $h = 10^{-5}$, we arrive at the situation shown in figure 2 by the dashed line. We must initially take the Briggs–Bers temporal inversion contour $\mathcal{C}_\omega$ below $\omega(k)$ for real k in order to satisfy causality, while the $\mathcal{C}_k$ contour is taken along the real k axis. In this case, a suitable starting contour is seen from figure 2 to be $\mathrm{Im}(\mathcal{C}_\omega) = -100$. We then deform this contour back onto the real ω axis, taking care to deform the $\mathcal{C}_k$ contour to avoid any modes in the k plane crossing it. If, however, a pinch frequency ω_p exists for which two modes in the k plane coincide and "pinch" the $\mathcal{C}_k$ contour, this deformation must stop. Briggs[3] showed that this gives rise to an absolute instability, present simultaneously upstream and downstream of the driver, that dominates the solution at large times. Writing (4) as $\Delta(k, \omega) = 0$, a pinch point occurs at a double root, given by $\partial\Delta/\partial k = 0$. The values of ω and k which simultaneously satisfy both of these constraints were found numerically using a two-dimensional Newton–Raphson iteration, with starting points located on a grid covering the relevant areas of the k- and ω-planes. The values of ω found are shown in figure 7. It remains to check which of these are modes from above the $\mathcal{C}_k$ contour colliding with modes from below $\mathcal{C}_k$ (corresponding to a pinch point), and which are modes from the same side of $\mathcal{C}_k$ colliding, for which we can move the $\mathcal{C}_k$ contour out of the way and therefore do not prevent us from continuing to deform the $\mathcal{C}_\omega$ contour. The majority of the double roots involves the collision of two modes on the same side of $\mathcal{C}_k$, and so do not correspond to a pinch points, as for example shown in figure 8(a). The dominant double roots that do correspond to pinch points are found to be $\omega_p = \pm 13 - 54\mathrm{i}$; the nature of this double-root is demonstrated to be a pinch point in figure 8(b).

If we had instead applied a naive application of the Briggs–Bers criterion as is common in the literature, involving, say, analytically continuing from $\mathrm{Im}(\omega) = -100$ to $\mathrm{Im}(\omega) = 0$ with $\mathrm{Re}(\omega) = 1$, we would arrive at something like figure 9. This shows the upper-right and far-right surface modes crossing the real k axis, and we would therefore have concluded that if the system were forced at a driving frequency of $\omega_f = 1$, these two modes would be present as right- and left-propagating convective instabilities respectively, and with frequency ω_f. This stability analysis is not complete, however, without first considering the possibility of absolute instability. In fact, we have shown that when excited at a frequency $\omega_f = 1$, the dominant contribution to the solution at large times is an absolute instability, which grows exponentially in time at the frequency $\omega_p = \pm 13 - 54\mathrm{i}$.

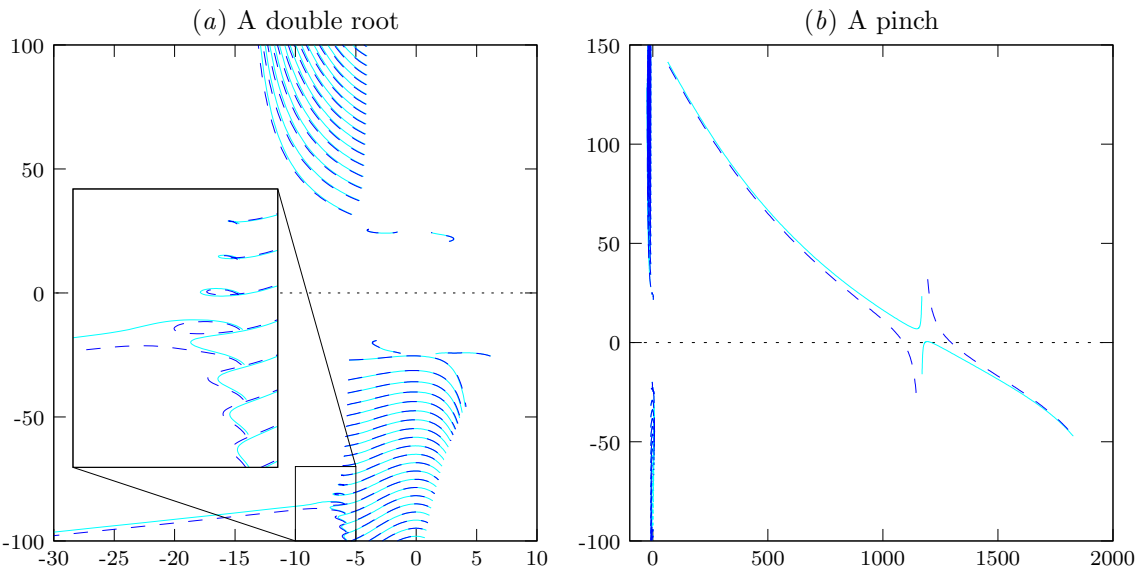

Figure 8. Trajectories in the k plane as $\mathrm{Im}(\omega)$ is varied with $\mathrm{Re}(\omega)$ fixed, for two double roots shown in figure 7. (*a*) One of the double roots labelled "Surface Mode" in figure 7, between $\mathrm{Re}(\omega) = 7.0$ (solid line) and $\mathrm{Re}(\omega) = 7.1$ (dashed line). (*b*) The absolute instability pinch between $\mathrm{Re}(\omega) = 13.0$ (solid line) and $\mathrm{Re}(\omega) = 12.9$ (dashed line).

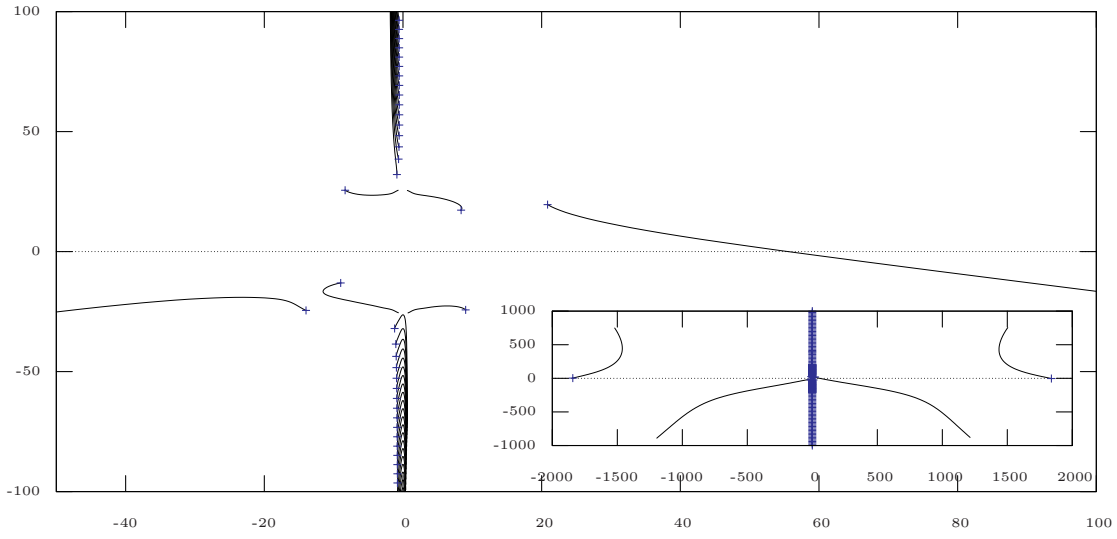

Figure 9. Trajectories of modes in the k-plane for $-100 \leq \mathrm{Im}(\omega) \leq 0$ with $\mathrm{Re}(\omega) = 1$, with crosses at $\mathrm{Im}(\omega) = 0$. Parameters are for air in aluminium (see table 1), with $b = 1$, $R = 3$, $h = 10^{-5}$, $U = 0.5$, and $m = 24$ (as for figure 7).

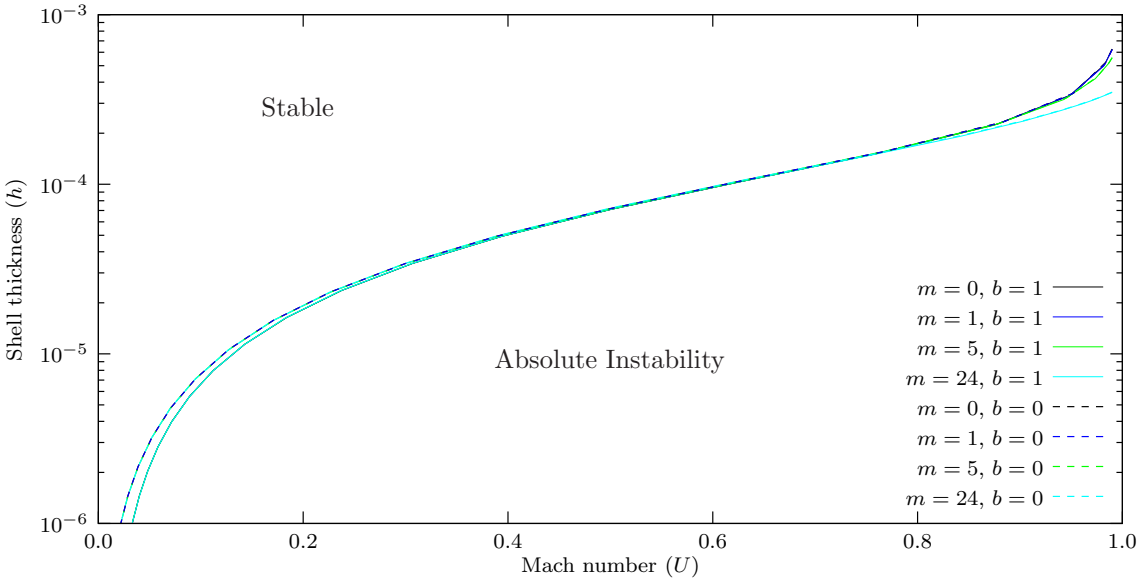

Figure 10. Values of h and U giving an absolute instability. The results are independent of R. Parameters are for an air-filled aluminium duct (see table 1).

C. The shell-thickness necessary for absolute-instability

The question now arises, how small a shell thickness is needed for there to be an absolute instability? By first finding the dominant pinch frequency ω_p, and then tracking this pinch frequency as h is varied, the critical shell thickness h_c giving $\mathrm{Im}(\omega_p) = 0$ may be found. For $h < h_c$ we have $\mathrm{Im}(\omega_p) < 0$, giving an absolute instability, while for $h > h_c$ we have $\mathrm{Im}(\omega_p) > 0$, and the $\mathcal{C}_\omega$ contour may be deformed onto the real ω axis, so that no absolute instability is present. Figure 10 plots these values of h_c for a variety of parameters; the amount of external damping, R, is found to have no effect on h_c, and so figure 10 only considers $R = 3$. For small U the dominant parameter is the Winkler foundation spring constant b, while the azimuthal order m plays little role. As U approaches unity the situation is reversed, and m becomes the dominant parameter, while b plays little role.

In all the cases investigated, the transition from $\mathrm{Im}(\omega_p) < 0$ to $\mathrm{Im}(\omega_p) > 0$ occurs in the same manner. Consider the double roots shown in figure 7. For a double root to correspond to a pinch, one mode must originate from the upper-half k-plane and one from the lower-half. Hence, at least one of these modes must cross the real k axis, shown as a solid line in figure 7 making two fingers in the lower-half ω-plane. As h is increased, these two fingers shrink, until at a certain value of h there are no modes with real k in the lower-half ω-plane, and so there can be no instabilities (either absolute or convective). The dominant pinch frequency ω_p is located towards the ends of these fingers, and the critical shell thickness h_c turns out to be exactly the value of h for which these fingers disappear from the lower-half ω-plane. This implies the interesting result that the system is either absolutely unstable or stable, and there is no possibility of the system supporting only convective, but not absolute, instabilities.

Another interesting feature is that the two fingers of $\omega(k)$ for real k shrink down to $\omega = 0$, and consequently the critical value of ω_p, defined as $\mathrm{Im}(\omega_p) = 0$, actually occurs at $\omega_p = 0$. Assuming this to always be the case, (11) implies that h_c is given by requiring $\Delta = \partial\Delta/\partial k = 0$, where

$$\Delta \equiv \left(k^2 + m^2/\beta^2\right)\left(\left({c_l}^2 d + b\right)/B + \left(k^2 + m^2\right)^2\right)^2 - \frac{U^4 k^4}{B^2\beta^2} \tag{13}$$

Note that setting $\omega_p = 0$ has eliminated the boundary damping R from (13), explaining why the curves in figure 10 are independent of R. If value of k for which $\omega_p = 0$ satisfies $k \gg m/\beta$ (which will turn out to be valid provided U is sufficiently far from unity), we may set $m = 0$ in (13) to leading order, to give

$$h_c = -\frac{b}{2{c_l}^2\rho_s} + \frac{1}{2}\sqrt{\left(\frac{b}{{c_l}^2\rho_s}\right)^2 + \left(\frac{9U^4}{(1-U^2){c_l}^4{\rho_s}^2}\right)^{2/3}}. \tag{14}$$

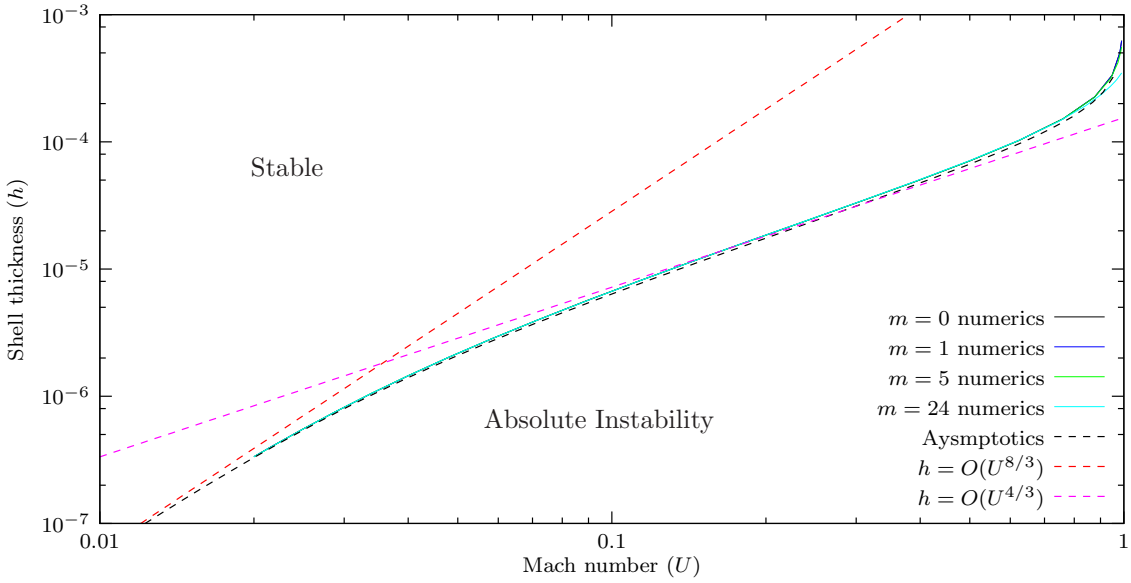

Figure 11. Comparison between asymptotic approximations and numerical results for h_c, for $b = 1$. Solid lines give the numerical results, and dashed lines give the asymptotics of (14) and the power laws derived from it.

If $U \ll 1$, this reduces to two cases, an $h_c = O(U^{8/3})$ power law if $U \ll U_c$ and an $h_c = O(U^{4/3})$ power law if $U \gg U_c$, given by

$$h_c \simeq \frac{{c_l}^2 \rho_s}{b} \left(\frac{9U^4}{8{c_l}^4 {\rho_s}^2} \right)^{2/3} \qquad \text{or} \qquad h_c \simeq \left(\frac{9U^4}{8{c_l}^4 {\rho_s}^2} \right)^{1/3} \qquad \text{where} \qquad U_c = \left(\frac{8b^3}{9{c_l}^2 \rho_s} \right)^{1/4}$$

This is because, for $U \ll U_c$, the Winkler foundation spring force b dominates the thin-shell spring force ${c_l}^2 d$, while for $U \gg U_c$ the thin-shell spring force dominates. Note that if $b = 0$, corresponding to no Winkler foundation spring force, the $h_c = O(U^{4/3})$ power law is universally valid for $U \ll 1$.

Figure 11 shows these three predictions, plotted against the values of h_c found numerically. As U approaches unity, the m^2/β^2 factor in (13) becomes significant, and the above asymptotics break down provided $m \neq 0$. However, for small and moderate U, the asymptotics derived above show a very good agreement to the numerical results, and the $U^{8/3}$ and $U^{4/3}$ scaling laws are clearly demonstrated.

D. Recovery of the mass–spring–damper boundary for small shell thicknesses

Since the thin-shell boundary model was introduced in order to regularize the mass–spring–damper boundary model, we now summarise the stability results of the thin-shell boundary in the limit $h \to 0$, which we know recovers the mass–spring–damper impedance. From figure 10, we know that the thin-shell boundary is absolutely unstable provided h is sufficiently small, with dominant frequency ω_p. As $h \to 0$, $\mathrm{Im}(\omega_p) \to -\infty$, so that for arbitrarily small shell thicknesses the absolute instability grows arbitrarily quickly. The pinch leading to this absolute instability occurs because two of the surface modes coincide and pinch the $\mathcal{C}_k$ contour, and one of these surface modes is a surface mode that disappears to infinity as $h \to 0$, as shown in figure 4(b). We therefore conclude that interpreting the mass–spring–damper as a thin shell of zero thickness, there is an absolute instability present of infinite temporal growth rate, and there are two surface modes that are at $k = \infty$. Of course, we knew already that, even for real k, the mass–spring–damper boundary supported arbitrarily large temporal growth rates, as shown in figure 2.

As a comparison between the thin-shell and mass–spring–damper boundaries for a naive Briggs–Bers application, consider figure 12. This appears to show the thin shell to be stable at this frequency and the mass–spring–damper boundary to admit a convective instability. However, as we have discovered, one must always consider the possibility of absolute instability in a Briggs–Bers analysis, and in fact for these parameters the thin shell is absolutely unstable with a dominant frequency $\omega_p = \pm 0.937 - 1.01\mathrm{i}$.

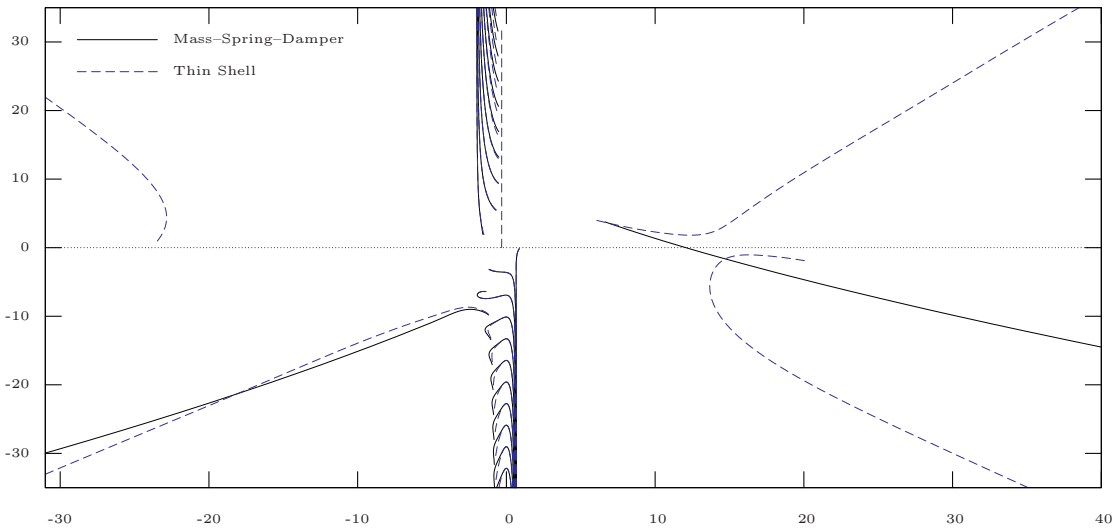

Figure 12. Comparison of Briggs–Bers trajectories in the k plane between a mass–spring–damper and thin-shell boundary, for $U = 0.5$, $m = 0$, $\omega = 1$. The mass–spring–damper has $b = 1$, $d = 0.1$, and $R = 1$, and the thin shell has $h = 1.75 \times 10^{-2}$ and $\nu = 0.33$ (and $c_l = 10$, $\rho_s = 5.7$, $b = 0$). These parameters correspond to figure 4 of ref. 2.

VI. Wiener–Hopf scattering

Recently, Rienstra & Peake[2] considered the scattering of an acoustic duct mode at a transition from a hard-wall to a locally-reacting boundary. As there was some question over the stability of the surface modes, they considered both stable and unstable cases. We now investigate how this scattering is altered by modelling the boundary as a thin shell.

Consider the duct shown in figure 3, which for $x < 0$ has a hard-wall boundary with boundary condition $\partial\phi/\partial r = 0$, while for $x > 0$ the boundary is a thin shell, as described by Flügge's equations in section IV. The thin-shell boundary is clamped at the intersection $x = 0$.

All quantities are assumed to be proportional to $\exp\{\mathrm{i}\omega t - \mathrm{i}m\theta\}$, and this factor will henceforth be dropped. A right-propagating mode in the hard-wall duct section has pressure p_{in}, given by

$$p_{\mathrm{in}}(x,r) = \exp\{-\mathrm{i}k_{\mathrm{in}}x\}\mathrm{J}_m(\alpha_{\mathrm{in}}r)/\mathrm{J}_m(\alpha_{\mathrm{in}}) \qquad {\alpha_{\mathrm{in}}}^2 = (\omega - Uk_{\mathrm{in}})^2 - {k_{\mathrm{in}}}^2 \qquad \mathrm{J}'_m(\alpha_{\mathrm{in}}) = 0$$

Since this mode does not satisfy the boundary condition for $x > 0$, as it encounters the boundary transition it scatters into other duct modes, some of which are reflected back upstream. In order to describe this scattering, we use a Wiener–Hopf technique.[17]

A. Deriving the Wiener–Hopf equation

The governing equations and boundary condition for the fluid give

$$\frac{\mathrm{D}^2\phi}{\mathrm{D}t^2} - \nabla^2\phi = 0, \qquad \text{subject to} \qquad \frac{\partial\phi}{\partial r} = \frac{\mathrm{D}w}{\mathrm{D}t} \qquad \text{at } r = 1, \tag{15}$$

where $w(x)$ is the radial displacement of the thin shell. We split the fluid pressure into the sum of the incoming imposed pressure and a scattering pressure, so that $p = -\mathrm{D}\phi/\mathrm{D}t = p_{\mathrm{in}} - \mathrm{D}\psi/\mathrm{D}t$, where ψ is the potential of the scattered wave.

In order to achieve a causal solution, and for the convergence of the integrals that follow, it turns out to be convenient to consider $\omega = \omega_r - \mathrm{i}\varepsilon$ with ω_r real and ε positive. Moreover, we require ε to be chosen such that $\mathrm{Im}(\omega(k)) > -\varepsilon$ for all real k. Since by definition of ω there are no modes with real k, there exists some positive δ such that the strip $\mathcal{D}$ given by $|\mathrm{Im}(k)| < \delta$ is free of any hard-wall or thin-shell modes. By applying

the Briggs–Bers criterion, for this complex frequency all modes that originate at $x = 0$ decay exponentially as $x \to \pm\infty$, and from the definition of $\mathcal{D}$ it follows that they decay at least as fast as $\exp\{-\delta|x|\}$. It will also turn out to be useful to require δ to be small enough so that $\omega/(U \pm 1)$, k_l, and k_t all lie outside $\mathcal{D}$. Eventually, we will analytically continue the solution obtained for this complex frequency to $\varepsilon = 0$.

The Fourier transform of ψ is given by

$$\tilde{\psi}(k, r) = \int_{-\infty}^{\infty} \psi(x, r) \mathrm{e}^{\mathrm{i}kx} \, \mathrm{d}x,$$

which, because of the choice of ε above, converges absolutely and is therefore analytic for k in $\mathcal{D}$. The Fourier-transformed differential equation (15) is solved as before in terms of Bessel's functions, giving $\tilde{\psi}(k, r) = A(k)\mathrm{J}_m(\alpha(k)r)$, where $A(k)$ is an as yet undetermined function representing the spectrum of the scattered wave, and $\alpha(k)^2 = (\omega - Uk)^2 - k^2$. The branch cuts for $\alpha(k)$ are taken parallel to the imaginary axis and away from the real axis, so that $\alpha(k)$ is analytic and $\mathrm{Re}(\alpha(k)) > 0$ in $\mathcal{D}$. These branch cuts will turn out to be unnecessary, as in section II, although this will only become apparent a posteriori.

For $x < 0$ the duct wall is hard and therefore $w(x) \equiv 0$. The Fourier transform of $w(x)$ is therefore given by the half-range transform

$$H^+(k) = \int_0^{\infty} w(x) \mathrm{e}^{\mathrm{i}kx} \, \mathrm{d}x,$$

which is an analytic function of k for $\mathrm{Im}(k) > -\delta$. The boundary condition (15) gives

$$\alpha(k)A(k)\mathrm{J}'_m(\alpha(k)) = \mathrm{i}(\omega - Uk)H^+(k), \tag{16}$$

yielding $A(k)$ in terms of the unknown function $H^+(k)$. Equation (15) is now satisfied, for any function $H^+(k)$, or equivalently for any boundary deflection $w(x)$. We have therefore solved for the motion in the fluid, although we have yet to impose the thin-shell equations on the solid boundary.

For a thin-shell boundary, the boundary deflection $w(x)$ is related to the fluid pressure $p(x, 1)$ at the boundary by Flügge's equations, the full-range Fourier transforms of which we have already seen in (7). For the half-range Fourier transforms, note that

$$\int_0^{\infty} f'(x) \mathrm{e}^{\mathrm{i}kx} \, \mathrm{d}x = -f(0) - \mathrm{i}k \int_0^{\infty} f(x) \mathrm{e}^{\mathrm{i}kx} \, \mathrm{d}x$$

assuming appropriate decay at infinity (guaranteed by our choice of ε). Using the fact that the thin shell is clamped at $x = 0$, so that $w(0) = w'(0) = u(0) = v(0) = 0$, the half-range Fourier transforms give

$$\int_0^{\infty} p(x, 1) \mathrm{e}^{\mathrm{i}kx} \, \mathrm{d}x = \mathrm{i}\omega Z_1(k) H^+(k) + \mathrm{i}\omega Z_0(k), \tag{17}$$

where

$$\mathrm{i}\omega Z_1(k) = {\mathrm{c}_l}^2 d + b + \mathrm{i}\omega R - d\omega^2 + B\left(k^2 + m^2\right)^2 - {\mathrm{c}_l}^2 d \frac{{A_1}^2 a_{22} - 2A_1 A_2 a_{12} + {A_2}^2 a_{11}}{\left(\dfrac{\omega^2}{{\mathrm{c}_l}^2} - (k^2 + m^2)\right)\left(\dfrac{\omega^2}{{\mathrm{c}_l}^2} - \dfrac{1 - \nu}{2}(k^2 + m^2)\right)}, \tag{18}$$

$$\mathrm{i}\omega Z_0(k) = \mathrm{i}{\mathrm{c}_l}^2 d \frac{A_1 C_1 a_{22} - (A_1 C_2 + A_2 C_1) a_{12} + A_2 C_2 a_{11}}{\left(\dfrac{\omega^2}{{\mathrm{c}_l}^2} - (k^2 + m^2)\right)\left(\dfrac{\omega^2}{{\mathrm{c}_l}^2} - \dfrac{1 - \nu}{2}(k^2 + m^2)\right)} + \mathrm{i}BC_3 k - BC_4, \tag{19}$$

and the constants C_1 to C_4 are given by

$$C_1 = u'(0) - \frac{h^2}{12} w''(0), \qquad C_2 = \frac{1 - \nu}{2} v'(0),$$
$$C_3 = \left(1 - \frac{h^2}{12}\right) w''(0) - C_1, \qquad C_4 = \left(1 - \frac{h^2}{12}\right) w'''(0) + 2\mathrm{i}mC_2.$$

The equality $u''(0) = w'''(0)h^2/12 + \mathrm{i}mv'(0)(1 + \nu)/2$, implied by the axial component of Flügge's equations, has been used to write C_4 in the given form. We shall consider these constants later, but for the moment

we assume their values to be known. By considering the half-range transform of the scattered pressure at the boundary,

$$P^-(k) = \int_{-\infty}^{0} -\frac{\mathrm{D}\psi}{\mathrm{D}t}(x,1)\mathrm{e}^{\mathrm{i}kx}\,\mathrm{d}x,$$

which is analytic for $\mathrm{Im}(k) < \delta$, and by noting that the half-range Fourier transform of $p_{\mathrm{in}}(x,1)$ is

$$\int_{0}^{\infty} p_{\mathrm{in}}(x,1)\mathrm{e}^{\mathrm{i}kx}\,\mathrm{d}x = \mathrm{i}/(k-k_{\mathrm{in}}),$$

equation (17) may be transformed to become

$$P^-(k) - \mathrm{i}/(k-k_{\mathrm{in}}) + \mathrm{i}\omega Z_0(k) = H^+(k)K(k), \qquad K(k) = \frac{(\omega - Uk)^2\mathrm{J}_m(\alpha(k))}{\alpha(k)\mathrm{J}'_m(\alpha(k))} - \mathrm{i}\omega Z_1(k). \tag{20}$$

$K(k)$ is the Wiener–Hopf kernel, and (20) forms the Wiener–Hopf problem.

B. Solving the Wiener–Hopf equation

In order to solve this Wiener–Hopf problem, we must first investigate where the poles and zeros of $K(k)$ lie. $K(k)$ has poles which are zeros of $\mathrm{J}'_m(\alpha(k))$, zeros of $\alpha(k)$, or poles of $\mathrm{i}\omega Z_1$. Zeros of $\mathrm{J}'_m(\alpha(k))$ correspond to hard-wall duct modes, while the poles of $\mathrm{i}\omega Z_1$ are due to the determinant of (7b) being zero, and occur at $\pm k_l$ and $\pm k_t$. The zeros of $K(k)$ are given by the zeros of $\chi(k)$, where

$$\chi(k) = (\omega - Uk)^2\mathrm{J}_m(\alpha(k)) - \mathrm{i}\omega Z_1(k)\alpha(k)\mathrm{J}'_m(\alpha(k)), \tag{21}$$

and hence correspond to duct modes for a duct boundary with impedance Z_1 (c.f. equation 4). Hence, by definition of ε, the strip $\mathcal{D}$ contains no poles or zeros of $K(k)$.

As described in appendix B, $K(k)$ may therefore be factorized into $K(k) = K^+(k)/K^-(k)$, where $K^+(k)$ is analytic for $\mathrm{Im}(k) > -\delta$, and $K^-(k)$ is analytic for $\mathrm{Im}(k) < \delta$. Similarly (although more simply), $\mathrm{i}\omega Z_0(k)K^-(k)$ may be split into $F^-(k) + F^+(k)$. Substituting these factorizations into (20) yields

$$P^-(k)K^-(k) - \frac{\mathrm{i}\left(K^-(k) - K^-(k_{\mathrm{in}})\right)}{k-k_{\mathrm{in}}} + F^-(k) = H^+(k)K^+(k) + \frac{\mathrm{i}K^-(k_{\mathrm{in}})}{k-k_{\mathrm{in}}} - F^+(k). \tag{22}$$

The left hand side is analytic for $\mathrm{Im}(k) < \delta$, while the right hand side is analytic for $\mathrm{Im}(k) > -\delta$. Hence, (22) defines an entire function $E(k)$.

From appendix B, the following asymptotic behaviour is found as $|k| \to \infty$ in the regions of analyticity:

$$K^-(k) = O\left(k^{-2}\right), \qquad F^-(k) = O\left(k^{-1}\right), \qquad K^+(k) = O\left(k^{2}\right), \qquad F^+(k) = O\left(k^{-1}\right).$$

Using integration by parts, if $g(x) = O(x^n)$ as $x \to 0$ then the half-range Fourier transform of g is $O(k^{-(n+1)})$ as $|k| \to \infty$. Assuming the fluid pressure at the boundary at $x = 0$ to be finite, this gives $P^-(k) = O(k^{-1})$, while the clamped boundary conditions $w(0) = w'(0) = 0$ imply $H^+(k) = O(k^{-3})$. Hence, both the left and right hand sides of (22) are $O(k^{-1})$ as $|k| \to \infty$, and so by Liouville's theorem the entire function $E(k) \equiv 0$.

Setting the right hand side of (22) to zero gives an equation for $H^+(k)$, from which (16) gives the scattering wave spectrum $A(k)$, and hence

$$p(x,r) = p_{\mathrm{in}}(x,r) + \frac{1}{2\pi\mathrm{i}}\int_{-\infty}^{\infty} \frac{(\omega - Uk)^2\mathrm{J}_m(\alpha(k)r)}{\alpha(k)\mathrm{J}'_m(\alpha(k))K^+(k)}\left[\frac{K^-(k_{\mathrm{in}})}{k-k_{\mathrm{in}}} + \frac{\mathrm{i}R_l}{k-k_l} + \frac{\mathrm{i}R_t}{k-k_t}\right]\mathrm{e}^{-\mathrm{i}kx}\,\mathrm{d}k, \tag{23}$$

where

$$\begin{aligned} R_l &= \frac{\mathrm{i}{\mathrm{c}_l}^2 dK^-(k_l)}{2k_l\omega^2/{\mathrm{c}_l}^2}\left({k_l}^2\left(\nu + \frac{h^2\omega^2}{12{\mathrm{c}_l}^2}\right) + m^2\right)(k_lC_1 + mC_2), \\ R_t &= \frac{\mathrm{i}{\mathrm{c}_l}^2 dK^-(k_t)}{2\omega^2/{\mathrm{c}_l}^2} m\left(1 - \nu + \frac{h^2\omega^2}{12{\mathrm{c}_l}^2}\right)(k_tC_2 - mC_1). \end{aligned} \tag{24}$$

are from $F^+(k)$ (see equation 30 in appendix B).

Since the integrand is $O(k^{-2})$ as $|k| \to \infty$, for $x < 0$ the integration contour may be closed in the upper half plane and Jordan's lemma applied. Technically, we must deform this contour around the branch

cut of α in the upper half plane. However, since $\mathrm{J}_m(\alpha r)/(\alpha \mathrm{J}'_m(\alpha))$ is a meromorphic function of α^2, the integrand is identical on either side of the branch cut, and the contribution from integrating around the branch cut therefore vanishes. The singularity at $\alpha = 0$ corresponds to a removable singularity for $m \neq 0$, while for $m = 0$ it is included in the following analysis provided it is taken that $m^2/\alpha^2 = 0$. The integral is therefore $2\pi\mathrm{i}$ times the sum of the residues of the integrand in the upper half plane. These poles are given by $\mathrm{J}'_m(\alpha(k)) = 0$, and so correspond to hard-wall duct modes. Denoting the j^{th} positive root of $\mathrm{J}'_m(\alpha) = 0$ by $\alpha_{jm} = \alpha(k_{jm})$ with $\mathrm{Im}(k_{jm}) > 0$, for $x < 0$ the pressure is given by

$$p(x,r) = \frac{\mathrm{J}_m(\alpha_{\mathrm{in}} r)}{\mathrm{J}_m(\alpha_{\mathrm{in}})} \exp\{-\mathrm{i}k_{\mathrm{in}} x\} + \sum_{j=1}^{\infty} R_{jm} \frac{\mathrm{J}_m(\alpha_{jm} r)}{\mathrm{J}_m(\alpha_{jm})} \exp\{-\mathrm{i}k_{jm} x\},$$

$$R_{jm} = \frac{(\omega - U k_{jm})^2}{(U\omega + \beta^2 k_{jm})(1 - m^2/{\alpha_{jm}}^2) K^+(k_{jm})} \left[\frac{K^-(k_{\mathrm{in}})}{k_{jm} - k_{\mathrm{in}}} + \frac{\mathrm{i}R_l}{k_{jm} - k_l} + \frac{\mathrm{i}R_t}{k_{jm} - k_t} \right].$$

Similarly, for $x > 0$ the integration contour in (23) may be closed in the lower half plane and Jordan's lemma applied. Writing $\alpha \mathrm{J}'_m(\alpha) K^+(k)$ as $K^-(k)\chi(k)$, where $\chi(k)$ is given in (21), the poles of the integrand of (23) are given by zeros of $\chi(k)$, and therefore correspond to duct modes for a duct boundary with impedance Z_1. The pole at k_{in} exactly cancels the incoming pressure p_{in}. The two poles at k_l and k_t correspond to zeros of the determinant (7b) and so are also poles of $\chi(k)$, and the integrand therefore has removable singularities at these points. Denoting the j^{th} zero of $\chi(k)$ by τ_{jm} with $\mathrm{Im}(\tau_{jm}) < 0$, the pressure for $x > 0$ is given by

$$p(x,r) = \sum_{j=1}^{\infty} T_{jm} \frac{\mathrm{J}_m(\alpha(\tau_{jm}) r)}{\mathrm{J}_m(\alpha(\tau_{jm}))} \exp\{-\mathrm{i}\tau_{jm} x\},$$

$$T_{jm} = -\frac{(\omega - U\tau_{jm})^2 \mathrm{J}_m(\alpha(\tau_{jm}))}{K^-(\tau_{jm})\chi'(\tau_{jm})} \left[\frac{K^-(k_{\mathrm{in}})}{\tau_{jm} - k_{\mathrm{in}}} + \frac{\mathrm{i}R_l}{\tau_{jm} - k_l} + \frac{\mathrm{i}R_t}{\tau_{jm} - k_t} \right].$$

We have now completely derived the solution within the fluid as a sum of duct modes. In the hard-wall half of the duct ($x < 0$), the fluid pressure is the sum of the inbound acoustic mode and reflected hard-wall modes with reflection coefficients R_{jm}. In the thin-shell half of the duct ($x > 0$), the fluid pressure is the sum of thin-shell modes with transmission coefficients T_{jm}. However, there is still the question of the four constants C_1 to C_4.

C. Determining the constants C_1 to C_4

By examining (23), we find that the dependence of the solution on the constants C_1 to C_4 occurs only through R_l and R_t, which themselves depend only on C_1 and C_2 and are independent of C_3 and C_4. In fact C_3 and C_4 may be calculated (in terms of C_1 and C_2) from our solution for H^+, since by integrating by parts,

$$H^+(k) = -\mathrm{i}w''(0)/k^3 + w'''(0)/k^4 + O(k^{-5}) \qquad \text{as } k \to \infty, \tag{25}$$

giving $w''(0)$ and $w'''(0)$, and hence C_3 and C_4. This is possible because, in determining H^+, we assumed the pressure to be bounded at $x = 0$, implying $P^-(k) = O(k^{-1})$ as $|k| \to \infty$. In general, however, setting the left hand side of (22) to zero gives $P^-(k) = O(k)$. Satisfying the finite pressure assumption therefore requires the constants C_3 and C_4 to be chosen such that

$$-\frac{\mathrm{i}K^-(k_{\mathrm{in}})}{k - k_{\mathrm{in}}} + F^+(k) = \mathrm{i}\omega Z_0 K^-(k) + O(k^{-3}),$$

and this can be shown to give the same values of C_3 and C_4 as (25). This may be interpreted as the shell bending at $x = 0$ in the only way that does not necessitate an infinite pressure in the fluid at the boundary. As C_3 and C_4 do not appear in the solution (23), it is never necessary to solve the above equations to calculate C_3 and C_4, and we may now forget about C_3 and C_4 completely.

We now turn our attention to the constants C_1 and C_2, which we determine by imposing causality. The inversion contour in (23) is chosen along the real k axis within the strip $\mathcal{D}$. By definition of ε, the Briggs–Bers criterion shows that this gives the causal solution to a disturbance in the fluid originating at $x = 0$.

However, the solid waves in the boundary with axial wavenumbers $\pm k_l$ and $\pm k_t$ are decoupled from w and produce no disturbance in the fluid for $x > 0$. It is therefore necessary to impose a further condition that no solid waves are inbound in the boundary from $x = +\infty$. The half-range Fourier transforms of the axial and azimuthal boundary displacements $u(x)$ and $v(x)$ for $x > 0$ are denoted $U^+(k)$ and $V^+(k)$, and are given by the half-range version of (7b) as

$$\begin{pmatrix} U^+ \\ V^+ \end{pmatrix} = \frac{1}{a_{11}a_{22} - {a_{12}}^2} \begin{pmatrix} a_{22} & -a_{12} \\ -a_{12} & a_{11} \end{pmatrix} \begin{pmatrix} -\mathrm{i}A_1 H^+ - C_1 \\ -\mathrm{i}A_2 H^+ - C_2 \end{pmatrix}. \tag{26}$$

This shows that $U^+(x)$ and $V^+(k)$ are $O(k^{-2})$ as $|k| \to \infty$. Taking the inversion contours for $u(x)$ and $v(x)$ above all poles of U^+ and V^+, Jordan's lemma may therefore be applied to give $u \equiv v \equiv 0$ for $x < 0$, while for $x > 0$, u and v are given as a sum of residues. In general, the poles of U^+ and V^+ are those of H^+. The zeros of the determinant $a_{11}a_{22} - {a_{12}}^2$, which occur when $k = \pm k_l$ or $k = \pm k_t$, lead to four additional poles of U^+ and V^+ which correspond to two inbound and two outbound solid boundary waves. In order that there be no incoming waves, it is required that the poles of U^+ and V^+ at both $-k_l$ and $-k_t$ have zero residue (recall that we chose k_l and k_t so as to represent right-propagating waves). While this would appear to be four conditions, the singularity of the matrix at these points reduces this requirement to two conditions,

$$\begin{aligned} k_l \left(\mathrm{i}A_1(-k_l)H^+(-k_l) + C_1\right) - m \left(\mathrm{i}A_2(-k_l)H^+(-k_l) + C_2\right) = 0, \\ m \left(\mathrm{i}A_1(-k_t)H^+(-k_t) + C_1\right) + k_t \left(\mathrm{i}A_2(-k_t)H^+(-k_t) + C_2\right) = 0. \end{aligned}$$

Since $H^+(k)$ is a linear function of C_1 and C_2, so too are the above two equations. Satisfying them specifies the constants C_1 and C_2 (which in turn specifies $u'(0)$ and $v'(0)$), and ensures that the only permissible solid boundary waves are those that propagate outward from $x = 0$.

It is interesting to note that, in fact, the solid boundary waves that propagate outward from $x = 0$ are not excited either. This is because these two modes, which correspond to the other two zeros of the determinant in (26) at $k = k_l$ and $k = k_t$, both have zero residue for any choice of C_1 and C_2. This may be seen by evaluating H^+ at k_l and k_t to give

$$H^+(k_l) = \mathrm{i}\frac{k_l C_1 + mC_2}{k_l A_1(k_l) + mA_2(k_l)} \qquad \text{and} \qquad H^+(k_t) = \mathrm{i}\frac{mC_1 - k_t C_2}{mA_1(k_t) - k_t A_2(k_t)},$$

and then substituting this into (26). The poles at k_l and k_t therefore correspond to removable singularities, and once C_1 and C_2 have been chosen as above so that the poles at $-k_l$ and $-k_t$ also correspond to removable singularities, the only poles of U^+ and V^+ are those of H^+. The wave scattering is therefore seen to excite none of the solid waves in the thin shell, although it can and in general will excite the quasi-solid surface modes in the fluid.

The values of all four constants C_1 to C_4 have now been specified, giving a unique solution, with the only assumptions being bounded pressure and causality. Since the thin shell was assumed clamped at $x = 0$, $w(0) = w'(0) = 0$, and hence the surface streamline is $O(x^2)$ as $x \to 0$.

D. Some examples

We now consider some scattering examples, which were numerically evaluated using the modal sums given above. The hard-wall and thin-shell wavenumbers k_{jm} and τ_{jm} were calculated using a Newton–Raphson iteration on the relevant dispersion relations, while the split functions K^+ and K^- were calculated by numerically integrating (29) from appendix B. Numerically, we take $\varepsilon = 0$, and deform the integration contours and the strip $\mathcal{D}$ away from the real k-axis in such a way that this gives the correct analytic continuation from ε as chosen above. That is, we choose the integration contours and the strip $\mathcal{D}$ such that modes above them are left-propagating, while modes below are right-propagating, exactly as for the Briggs–Bers stability criterion.

Figure 13 shows the numerically calculated hard-wall and thin-shell poles in the k-plane for an air-filled aluminium duct of 1m radius and 1mm shell thickness, with ω and m as appropriate for the BPF in an aeroengine intake.[14] The Briggs–Bers stability analysis of figure 6 has been superimposed on figure 13,

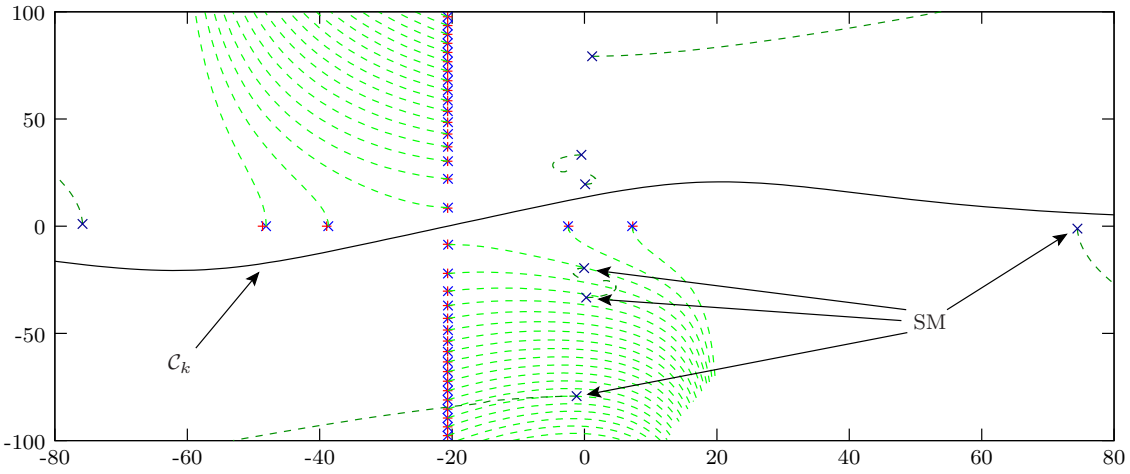

Figure 13. Duct modes in the k-plane for hard-wall (+) and thin-shell (×) boundaries. Surfaces modes present for $x > 0$ are labelled SM. The dashed lines show the Briggs–Bers trajectories of the modes. Parameters are for an air-filled aluminium duct (see table 1) with $R = 3$, $b = 1$, $h = 10^{-3}$, $\omega = 31$, $U = 0.5$, and $m = 24$.

showing the motion of the thin-shell modes as ε is varied, and demonstrating that the contour $\mathcal{C}_k$ gives the correct analytic continuation. The equation of this curve[2] is

$$k = \frac{\omega}{1-U^2}\left(\xi - U + \mathrm{i}Y\frac{4(\xi/q)}{3+(\xi/q)^4}\right), \qquad \xi \in \mathbb{R}, \tag{27}$$

with in this case $Y = 0.5$ and $q = 1.0$. Figure 14 shows the scattering response to an inbound 1st radial order mode for this situation. The 1st radial order mode is the hard-wall duct mode with the most positive $\mathrm{Re}(k)$ shown in figure 13, and nearly coincides with it's equivalent thin-shell mode. Figures 14(a) and 14(b) show that the response to the inbound mode is dominated by the rightmost thin-shell mode, with little scattering or reflection taking place. Figure 14(c) plots contours of the pressure perturbation amplitude.

The previous example used realisable parameters for an actual aluminium thin shell, and found the thin shell to act almost exactly as a rigid duct, with very little scattering taking place. As a more interesting example to demonstrate the Wiener–Hopf technique, we now consider $U = 0.5$, $R = 0.5$, $b = 0$, $m = 1$, $\omega = 16$, and $h = 10^{-4}$. For these parameters, the thin-shell modes are distinctly different from their hard-wall counterparts, and so the scattering is more evident, while figure 10 shows that the boundary is still stable. The hard-wall and thin-shell modes in the k-plane are shown in figure 15, with the Briggs–Bers trajectories showing the $\mathcal{C}_k$ contour to have been chosen to give the correct analytic continuation. The simple $\mathcal{C}_k$ contour in (27) does not provide enough flexibility to do this, and so the more general contour given by

$$k = \frac{\omega}{1-U^2}\left[\xi - U + \mathrm{i}Y\frac{4(\xi/q)}{3+(\xi/q)^4}\left(1 - \frac{1+g}{1+g(\xi/f+1-U/f)^2}\right)\right], \qquad \xi \in \mathbb{R}$$

was used, with $Y = 1.0$, $q = 0.4$, $f = 0.1$, and $g = 0.1$.

Figure 16 shows the scattering response for the incoming 1st radial order mode labelled I_1 in figure 15. The surface modes play a major role near $x = 0$ in order to match the hard-wall and thin-shell solutions smoothly, although for large x these modes still have a negligible effect owing to their large $\mathrm{Im}(k)$ and corresponding fast exponential decay. For large positive x the dominant mode is the 1st radial order thin-shell mode. However, note also the comparably large coefficient for the 6th radial order reflected (left-propagating) mode labelled R_6, showing that both transmission and reflection are important in this situation. Figure 17(a) shows the amplitude of pressure oscillations, obtained from summing the above coefficients. In $x < 0$, the sum of two modes is prominently seen: the inbound 1st radial order I_1 mode (maximum amplitude at $r = 1$ and zero amplitude at $r = 0$), and the 6th radial order R_6 reflected mode (visible as six horizontal bands). Figure 17(b) shows a more detailed view around the boundary transition at $x = 0$ where the surface modes are important, and demonstrates the continuity between $x < 0$ and $x > 0$ which is less apparent from figure 17(a).

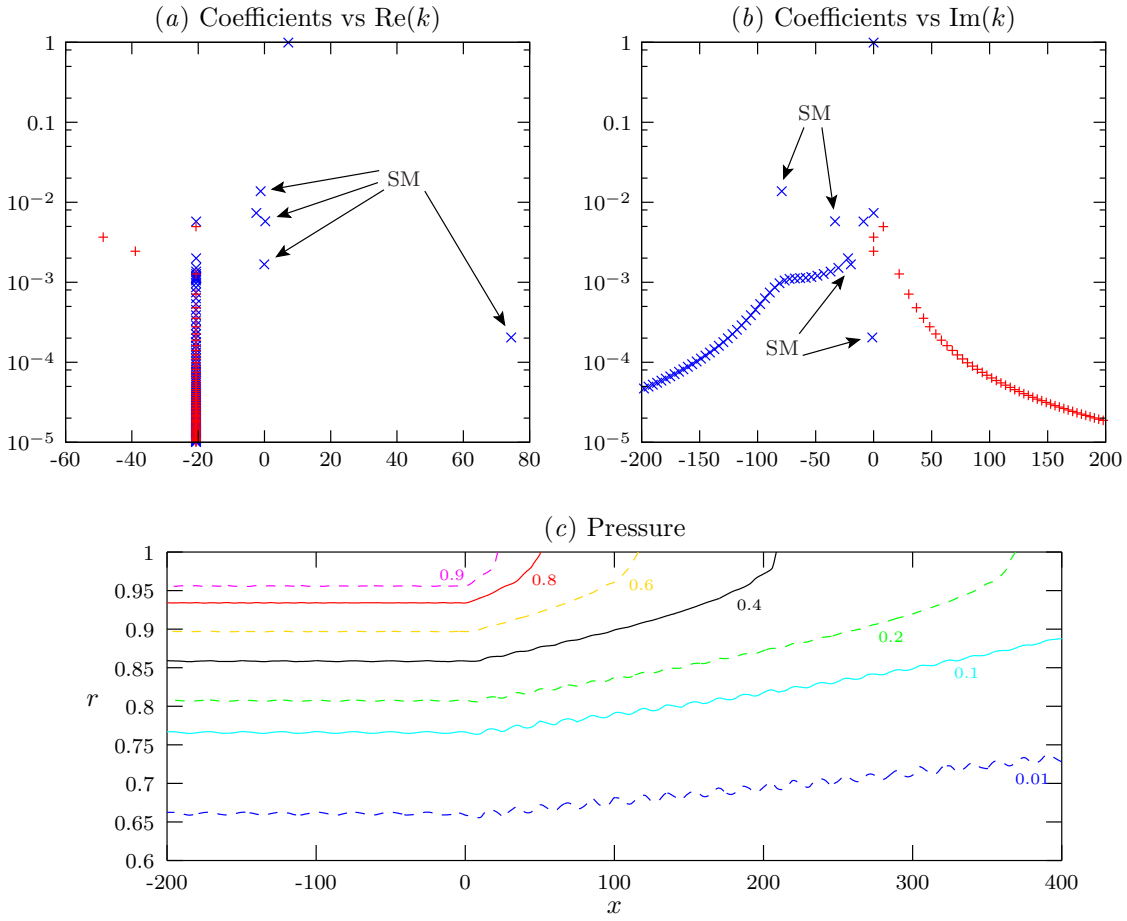

Figure 14. Scattering response to an inbound 1^{st} radial order mode. (*a*) and (*b*) plot the scattering coefficients $|R_{jm}|$ (+) and $|T_{jm}|$ (×) against $\mathrm{Re}(k)$ and $\mathrm{Im}(k)$. (*c*) shows the contours of the acoustic amplitude $|p(x,r)|$. Parameters are for an air-filled aluminium duct (see table 1) with $R = 3$, $b = 1$, $h = 10^{-3}$, $\omega = 31$, $U = 0.5$, and $m = 24$ (as for figure 13)

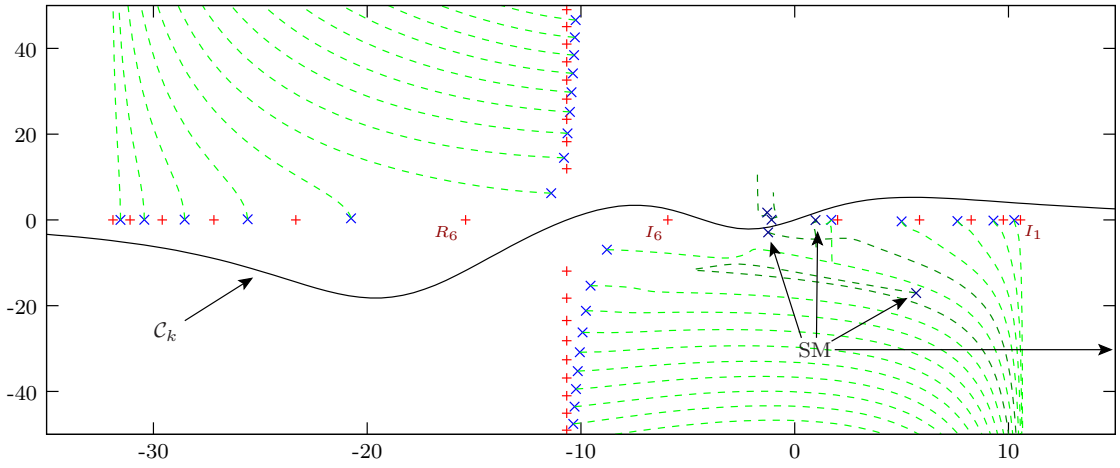

Figure 15. Duct modes in the k-plane for hard-wall (+) and thin-shell (×) boundaries, together with the Briggs–Bers trajectories (dashed lines) for the thin-shell modes. One surface mode is not shown owing to the scale used. The 1^{st} and 6^{th} radial order incoming (right-propagating) hard-wall modes and the 6^{th} radial order reflected (left-propagating) hard-wall mode are labelled I_1, I_6, and R_6 respectively. Parameters are for an air-filled aluminium duct (see table 1) with $R = 0.5$, $b = 0$, $h = 10^{-4}$, $\omega = 16$, $U = 0.5$, and $m = 1$.

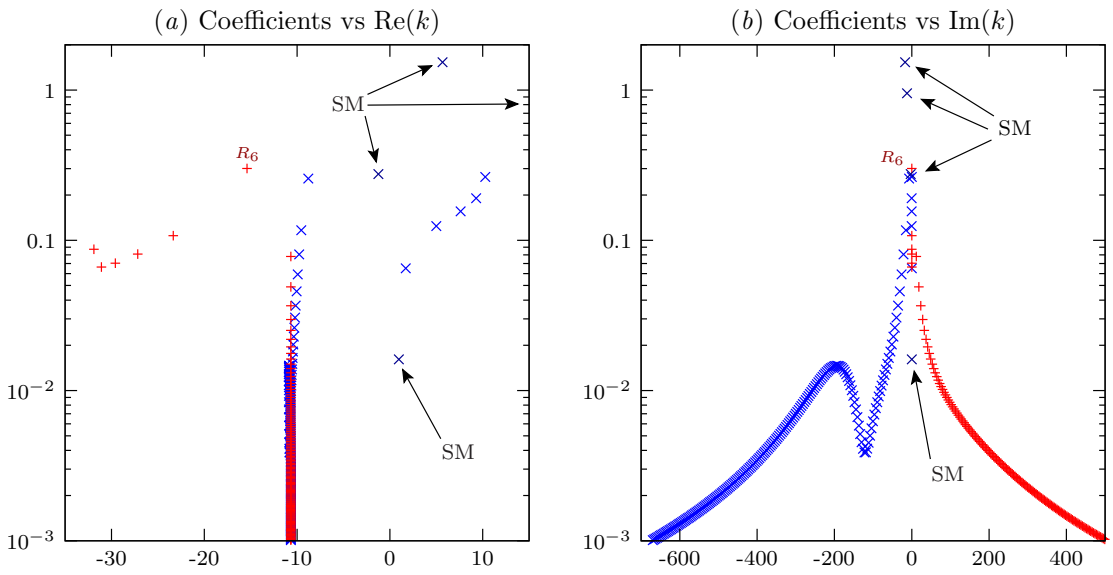

Figure 16. Scattering coefficients $|R_{jm}|$ (+) and $|T_{jm}|$ (×) due to an incoming 1^{st} radial order hard-wall mode I_1. Parameters are for an air-filled aluminium duct (see table 1) with $R = 0.5$, $b = 0$, $h = 10^{-4}$, $\omega = 16$, $U = 0.5$, and $m = 1$ (as for figure 15).

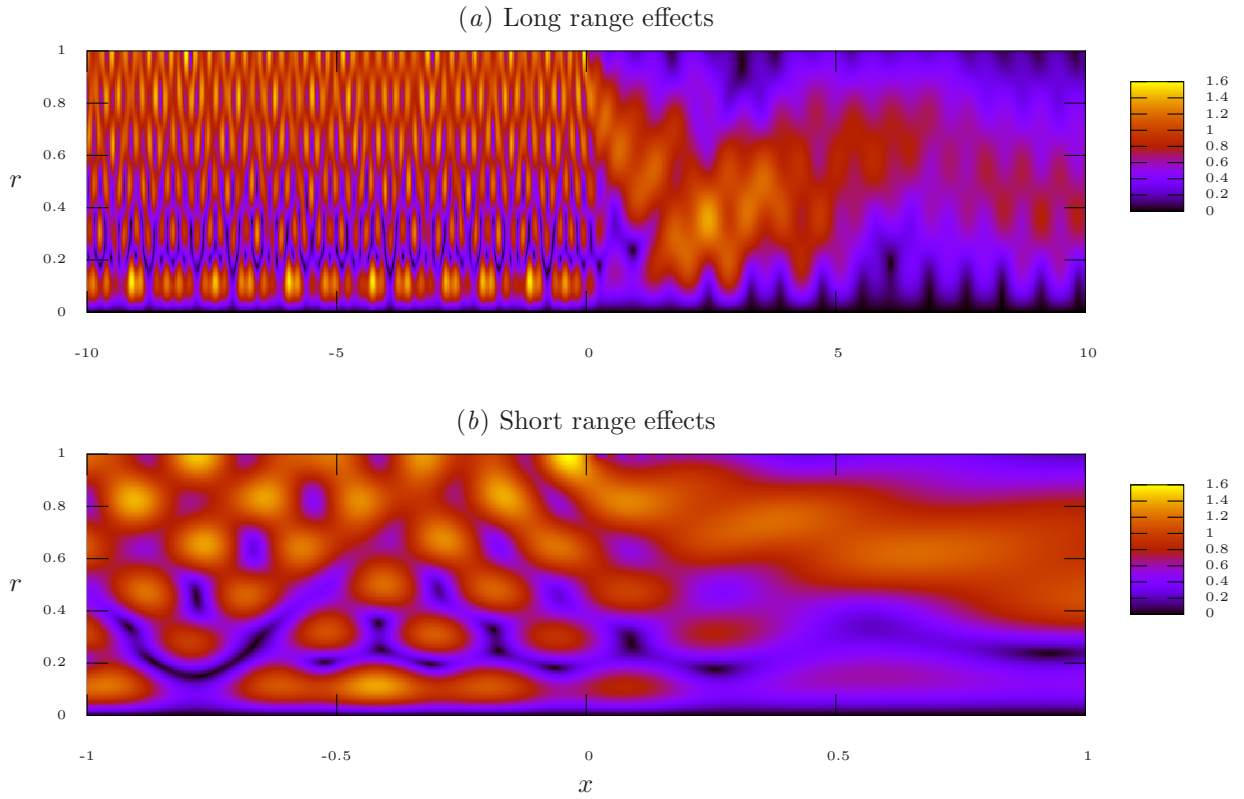

Figure 17. Amplitude of pressure oscillations $|p(r, x)|$ due to an inbound I_1 mode. (*b*) is a more detailed plot of (*a*) around the boundary transition at $x = 0$. Parameters are for an air-filled aluminium duct (see table 1) with $R = 0.5$, $b = 0$, $h = 10^{-4}$, $\omega = 16$, $U = 0.5$, and $m = 1$ (as for figure 16).

If, instead of I_1, the 6^{th} radial order mode I_6 is incident, the transmitted pressure disturbance almost completely disappears. Figure 18 shows the reflection and transmission coefficients for this case. Once again the surface modes are important in matching the solutions for $x < 0$ and $x > 0$, although their influence for large x is once again small. The dominant transmitted and reflected modes are both of 6^{th} radial order, although the thin-shell one of these is strongly damped. This is also evident from figure 19, which plots the amplitude of the pressure oscillations, and shows a standing 6^{th} radial order wave for $x < 0$ and virtually no transmitted wave in $x > 0$.

VII. Conclusion

A locally reacting mass–spring–damper (or a $\cot(\omega L)$ Helmholtz resonator) boundary model is inappropriate for stability analysis, since $\mathrm{Im}(\omega(k))$ is not bounded below for real k, and hence the proven Briggs–Bers criterion is inapplicable. In fact, problems for which $\mathrm{Im}(\omega(k))$ is not bounded below for real k are ill-posed, in that there are initial conditions for which the solution at $t = 0$ does not match with the solution at $t = \varepsilon$ in the limit $\varepsilon \to 0$. There may not even be a sensible answer to the question of spatial stability of such problems when excited with a time-harmonic forcing, although such problems are certainly temporally unstable for some initial conditions.

The problem is regularized by considering the boundary as a thin shell, as described by Flügge's equations. The influence of bending stiffness bounds $\mathrm{Im}(\omega(k))$ below for real k, enabling the Briggs–Bers criterion to be applied, while the mass–spring–damper model is obtained in the limit $h \to 0$. The ill-posedness mentioned above manifests itself as an absolute instability ω_p with $\mathrm{Im}(\omega_p) \to -\infty$ as $h \to 0$. Consequently, the solution to a time-harmonic forcing turned on at $t = 0$ grows arbitrarily fast in time as $h \to 0$. This also ties in with the surface modes' behaviour, since there are two thin-shell surface modes that tend to infinity as $h \to 0$, and that are not predicted by the the mass–spring–damper model.

The mass–spring–damper model was originally introduced[1] as a model of an acoustic lining in an aeroengine. Of course, the thin-shell boundary is a model of a different physical system, and we do not suggest that real acoustic liners should be modelled as thin shells. However, we have shown that by modifying the boundary condition for large k with the inclusion of bending stiffness, while retaining mass–spring–damper like behaviour for small k, a rigorous stability analysis is possible which leads to different conclusions about stability from those reached for the mass–spring–damper system. We suggest that, in order to perform a stability analysis on a model of an acoustic lining, the model needs to incorporate a k dependence in the impedance Z, such that $\mathrm{Im}(\omega(k))$ is bounded below.

For the Wiener–Hopf analysis using a mass–spring–damper boundary model, Rienstra & Peake[2] found that assuming all modes to be stable leads to an undesirable $O(x^{1/2})$ cusp in the surface streamline at $x = 0$. Considering one of the surface modes to be an instability gave an arbitrary constant, and this was chosen to satisfy the Kutta-like condition of $O(x^{3/2})$ smoothness for the surface streamline. Here, the boundary streamline is $O(x^2)$ without the inclusion of any instabilities, and indeed the Briggs–Bers criterion dictates that no instabilities should be present provided h is sufficiently large. The constants C_1 and C_2 could have been specified (incorrectly) by satisfying the Kutta-like condition of $O(x^4)$ smoothness of the surface streamline as $x \to 0$. However, this would have necessitated inbound solid waves in the boundary from $x = +\infty$, and would therefore not have given the correct causal solution to the problem of a wave inbound from $x = -\infty$ scattering off the sudden boundary change.

The Wiener–Hopf analysis above has been applied in three cases, two of which were chosen to demonstrate that reflection and scattering are possible for a hard-wall to thin-shell boundary transition. The first example may be interpreted as a model of the transition from a hard fan casing to a thin-shell nacelle casing for rearward-propagating tonal fan noise in an aeroengine, although in reality such a configuration would have an annular, rather than cylindrical, duct cross-section. For this case, the rotor-alone inbound mode propagated straight through without any significant scattering or reflection. A model of an aeroengine intake is obtained by taking U negative, since nowhere has it been assumed that $U > 0$. The results for $U = -0.5$ are very similar to those for $U = 0.5$, with the thin shell again behaving almost identically to a hard wall, and no significant scattering being seen.

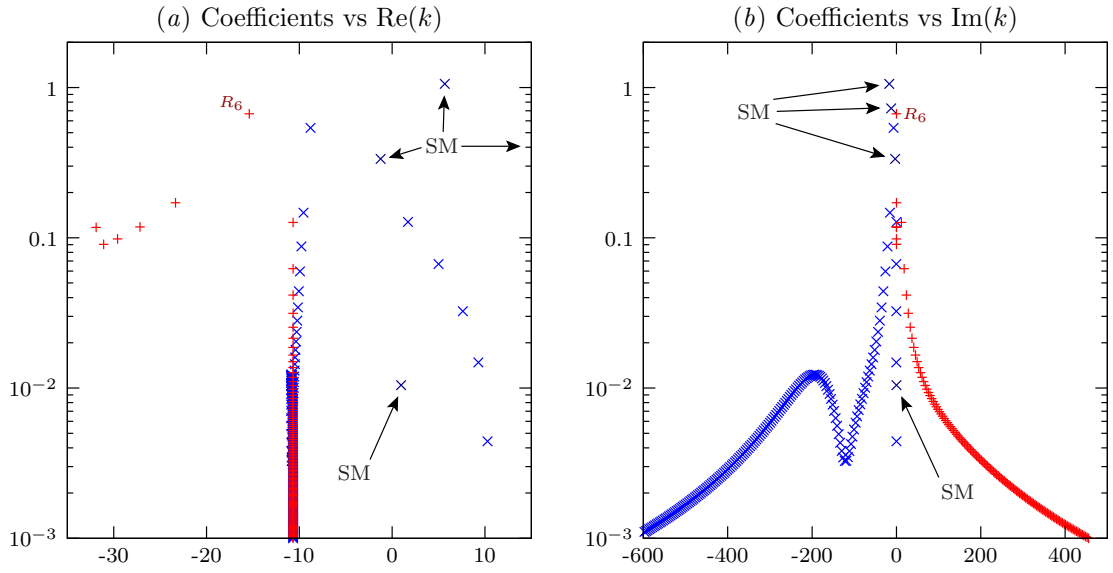

Figure 18. Scattering coefficients $|R_{jm}|$ (+) and $|T_{jm}|$ (×) due to an incoming 6^{th} radial order hard-wall mode I_6. Parameters are for an air-filled aluminium duct (see table 1) with $R = 0.5$, $b = 0$, $h = 10^{-4}$, $\omega = 16$, $U = 0.5$, and $m = 1$ (as for figure 15).

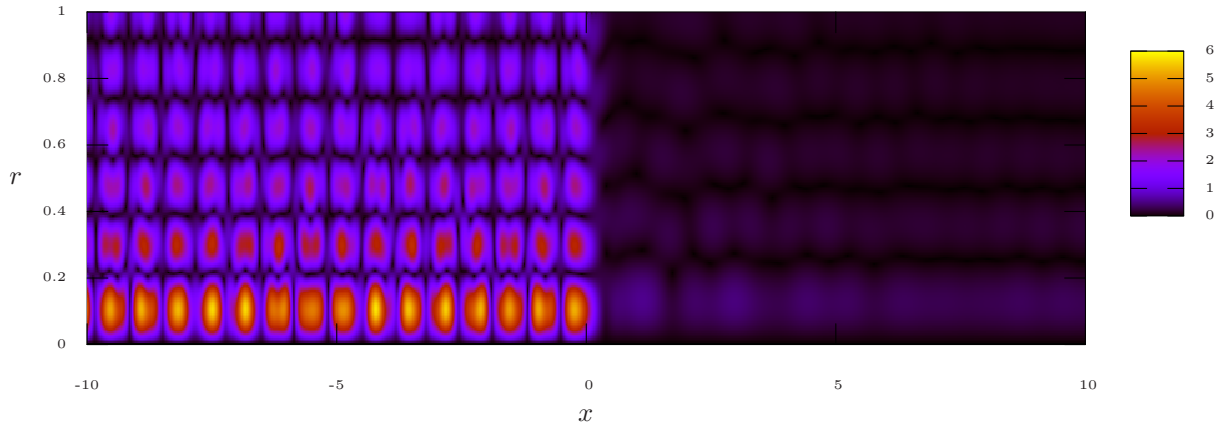

Figure 19. Amplitude of pressure oscillations $|p(r, x)|$ due to an inbound I_6 mode. Parameters are for an air-filled aluminium duct (see table 1) with $R = 0.5$, $b = 0$, $h = 10^{-4}$, $\omega = 16$, $U = 0.5$, and $m = 1$ (as for figure 18).

Acknowledgements

The authors are very grateful to Dr. P.D. Metcalfe and Dr. B. Veitch for several useful discussions. E.J. Brambley was supported by an EPSRC grant, and by Rolls-Royce plc under the University Gas Turbine Partnership Research Programme, and would like to thank both.

References

[1]Rienstra, S. W., "A Classification of Duct Modes based on Surface Waves," *Wave Motion*, Vol. 37, 2003, pp. 119–135.

[2]Rienstra, S. W. and Peake, N., "Modal Scattering at an Impedance Transition in a Lined Flow Duct," No. 2005-2852 in AIAA Paper, 2005.

[3]Briggs, R. J., *Electron-Stream Interaction with Plasmas*, chap. 2, MIT Press, 1964.

[4]Bers, A., "Space–Time Evolution of Plasma Instabilities — Absolute and Convective," *Basic Plasma Physics*, edited by A. A. Galeev and R. N. Sudan, Vol. 1 of *Handbook of Plasma Physics*, North-Holland, 1983, pp. 451–517.

[5]Jones, D. S. and Morgan, J. D., "The Instability of a Vortex Sheet on a Subsonic Stream under Acoustic Radiation," *Proc. Camb. Phil. Soc.*, Vol. 72, 1972, pp. 465–488.

[6]Jones, D. S. and Morgan, J. D., "A Linear Model of a Finite Amplitude Helmholtz Instability," *Proc. Roy. Soc. Lond.* A, Vol. 338, 1974, pp. 17–41.

[7]Crighton, D. G. and Leppington, F. G., "Radiation Properties of the Semi-Infinite Vortex Sheet: the Initial-Value Problem," *J. Fluid Mech.*, Vol. 64, 1974, pp. 393–414.

[8]Jones, D. S., "The Scattering of Sound by a Simple Shear Layer," *Phil. Trans. R. Soc. Lond.* A, Vol. 284, 1977, pp. 287–328.

[9]Rienstra, S. W., "Hydrodynamic Instabilities and Surface Waves in a Flow over an Impedance Wall," *Proc. IUTAM Symposium 'Aero- and Hydro-Acoustics'*, edited by G. Comte-Bellot and J. E. Ffowcs Williams, Springer, Heidelberg, 1985, pp. 483–490.

[10]Rienstra, S. W. and Tester, B. J., "An Analytic Green's Function for a Lined Circular Duct Containing Uniform Mean Flow," No. 2005-3020 in AIAA Paper, 2005.

[11]Gabard, G. and Astley, R. J., "Theoretical Model for Sound Radiated from Annular Jet Pipes: Far- and Near-Field Solutions," *J. Fluid Mech.*, Vol. 549, 2006, pp. 315–341.

[12]Goldstein, M. E., "Unsteady Vortical and Entropic Distortions of Potential Flows Round Arbitrary Obstacles," *J. Fluid Mech.*, Vol. 89, 1978, pp. 433–468.

[13]Myers, M. K., "On the Acoustic Boundary Condition in the Presence of Flow," *J. Sound Vib.*, Vol. 71, 1980, pp. 429–434.

[14]McAlpine, A. and Wright, M. C. M., "Acoustic Scattering by a Spliced Turbofan Inlet Duct Liner at Supersonic Fan Speeds," *J. Sound Vib.*, Vol. 292, 2006, pp. 911–934.

[15]Brambley, E. J. and Peake, N., "Classification of Aeroacoustically Relevant Surface Modes in Cylindrical Lined Ducts," *Wave Motion*, Vol. 43, 2006, pp. 301–310.

[16]Païdoussis, M. P., *Fluid-Structure Interactions Vol. 2*, Elsevier, 2004.

[17]Noble, B., *Methods based on the Wiener–Hopf Technique for the Solution of Partial Differential Equations*, Pergamon, 1958.

A. A comparison of stability criteria

In this appendix, we analyse the stability of the model problem

$$\frac{\partial G}{\partial t} + u\frac{\partial G}{\partial x} - \frac{\partial^2 G}{\partial x^2} - G = \delta(x)H(t)\exp\{\mathrm{i}\omega_f t\}, \tag{28}$$

for two values of the constant parameter u. This is a self-exciting advection–diffusion equation, and at $t = 0$ a harmonic point forcing is turned on at $x = 0$. Upon Fourier-transforming (28), we get

$$\Delta(k,\omega)\widetilde{G}(k,\omega) = -\mathrm{i}/(\omega - \omega_f), \qquad \text{where} \qquad \Delta(k,\omega) = \mathrm{i}(\omega - uk) + k^2 - 1.$$

Thus, the solution $G(x,t)$ is given as

$$G(x,t) = \frac{1}{4\pi^2\mathrm{i}}\int_{\mathcal{C}_\omega}\int_{\mathcal{C}_k}\frac{\exp\{\mathrm{i}\omega t - \mathrm{i}kx\}}{(\omega - \omega_f)\Delta(k,\omega)}\,\mathrm{d}k\,\mathrm{d}\omega.$$

Figure 20 shows the Briggs–Bers criterion applied to (28) for $u = 3$. Initially, we take the $\mathcal{C}_k$ contour along the real k axis, and the $\mathcal{C}_\omega$ contour anywhere below the image of $\mathrm{Im}(k) = 0$. We then deform the $\mathcal{C}_\omega$ contour upwards onto the real ω axis to pick up the pole contribution at $\omega = \omega_f$. In so doing, the zeros of $\Delta(k,\omega)$ in the k-plane move, and the $\mathcal{C}_k$ contour is deformed upwards to prevent the zeros from crossing the contour in order to maintain analyticity. The dashed arrowed lines show the motion of various parts of the $\mathcal{C}_\omega$ contour, and their images in the k-plane. The final shape of the $\mathcal{C}_k$ contour is shown in figure 20. By applying Jordan's lemma, zeros of $\Delta(k,\omega)$ (corresponding to poles of the k integrand) above $\mathcal{C}_k$ correspond to left-propagating modes, while zeros of $\Delta(k,\omega)$ below $\mathcal{C}_k$ correspond to right-propagating modes. It can be seen that for the range of frequencies $-3 < \omega < 3$, the k_- modes have crossed the real k axis but are below the $\mathcal{C}_k$ contour and therefore represent exponentially-growing right-propagating convective instabilities.

An alternative stability criterion,[9] which has recently found popularity in the literature,[1,2,10,11] is shown in figure 21. For this criterion, ω is analytically continued with $|\omega|$ fixed from $\arg(\omega) = -\pi/2$ to $\arg(\omega) = 0$. The dashed arrowed lines again show the motion of the modes as ω is varied, and those modes that finish in the upper-half k-plane that started in the lower half are alleged to be right-propagating instabilities. However, this criterion shows this happening only for $1 < |\omega| < 3$, in contradiction to the Briggs–Bers criterion. Since all the assumptions of the Briggs–Bers criterion[3,4] are justified for this example, the Briggs–Bers criterion gives the correct results, and hence this alternative criterion incorrectly predicts the stability of this model problem.

If instead we consider $u = 1$, the contrast between the two methods becomes more stark. For this case, as the $\mathcal{C}_\omega$ contour is deformed onto the real ω axis, k_+ and k_- coincide at $k_p = \mathrm{i}/2$ when $\omega = \omega_p = -3\mathrm{i}/4$ and pinch the $\mathcal{C}_k$ contour. We cannot therefore continue to deform this part of the $\mathcal{C}_\omega$ contour through ω_p whilst still maintaining the correct analytic continuation. Continuing to deform the $\mathcal{C}_\omega$ contour onto the real ω axis as far as possible yields the $\mathcal{C}_\omega{}'$ contour shown in figure 22. Note that some k_+ modes cross the real k axis and therefore correspond to convective instabilities, although the dominant large-time contribution comes from the part of the $\mathcal{C}_\omega$ contour with the most negative $\mathrm{Im}(\omega)$, which is at ω_p, leading to an absolute instability.

Figure 23 shows the alternative method applied to (28) with $u = 1$. Since no modes end up having crossed the real k axis because of the $\mathcal{C}_\omega$ deformation, this method predicts no instabilities at all, in stark contrast to the Briggs–Bers criterion. An erroneous result for this case is unsurprising, since this alternative criterion completely ignores the possibility of absolute instability.

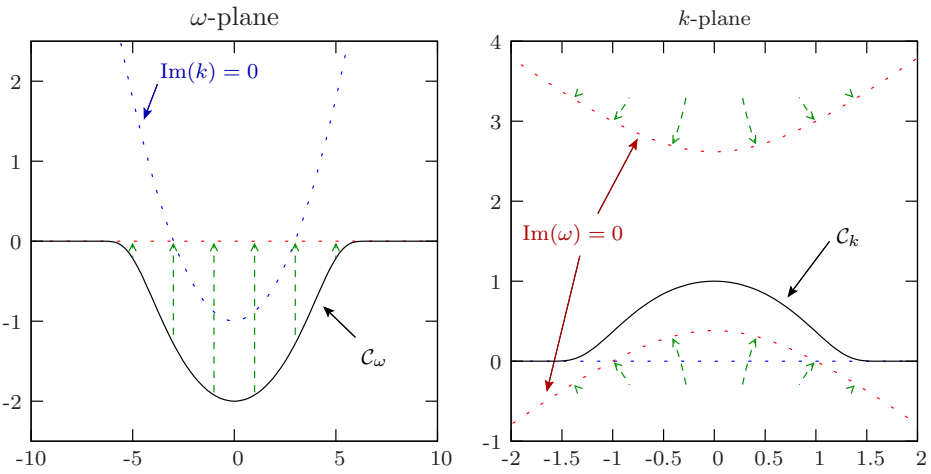

Figure 20. The Briggs–Bers criterion applied to (28) with $u = 3$. The $\mathcal{C}_\omega$ contour shown is the initial ω contour which is deformed onto the real axis. In so doing, the $\mathcal{C}_k$ contour is deformed off the real k axis into the contour shown, to avoid poles crossing the contour.

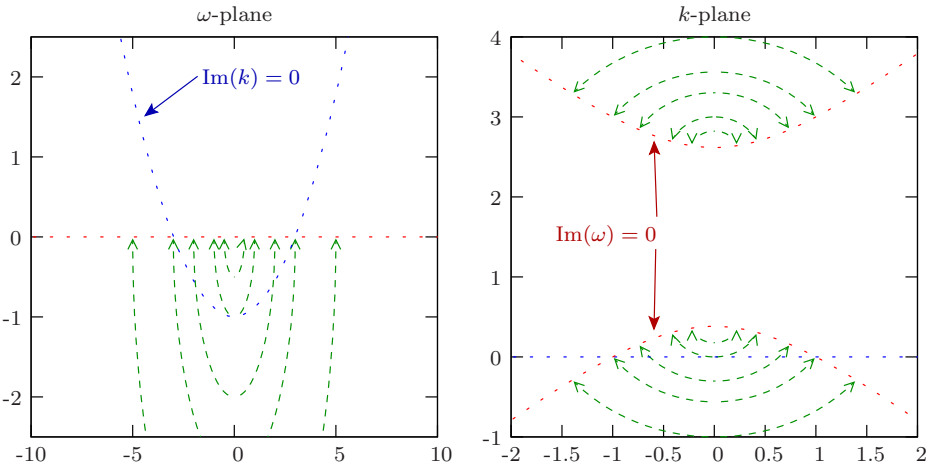

Figure 21. The method of ref. 9 applied to (28) with $u = 3$. The dashed arrowed lines show ω being deformed from purely imaginary to purely real with $|\omega|$ fixed, and the motion of the corresponding poles in the k-plane.

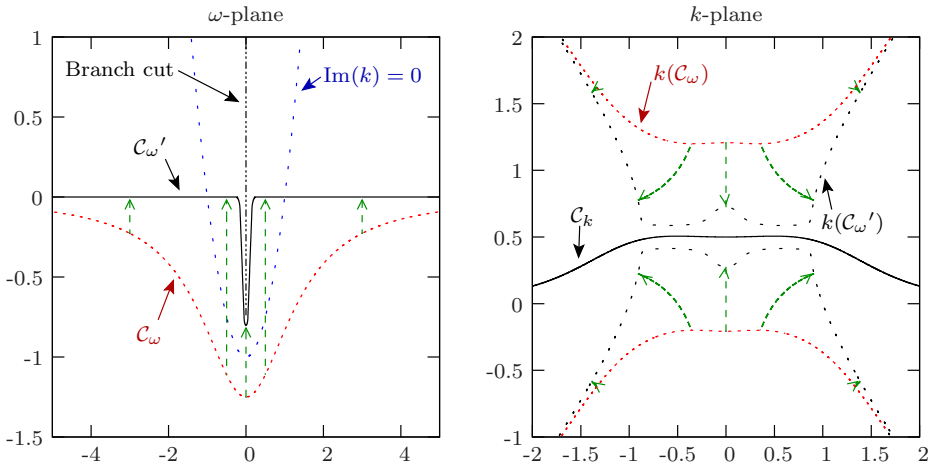

Figure 22. The Briggs–Bers criterion applied to (28) with $u = 1$. The $\mathcal{C}_\omega$ contour shown is the initial ω contour, which is deformed onto the real axis and around the branch cut into the contour $\mathcal{C}_\omega'$. In so doing, the $\mathcal{C}_k$ contour is deformed off the real k axis into the contour shown, to avoid poles crossing the contour.

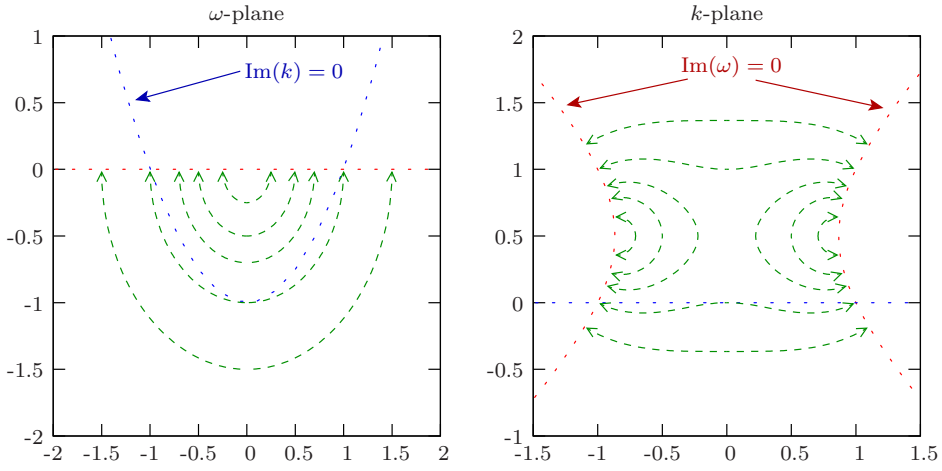

Figure 23. The method of ref. 9 applied to (28) with $u = 1$.

B. Details of the Wiener–Hopf scattering problem

In this appendix, we factorize $K(k)$, defined in (20), such that $K(k) = K^+(k)/K^-(k)$, where $K^+(k)$ is analytic and non-zero for $\mathrm{Im}(k) > -\delta$ and $K^-(k)$ is analytic and non-zero for $\mathrm{Im}(k) < \delta$. The method we follow is as described by Noble.[17] It follows from (18) that $K(k) = -B(1 - h^2/12)k^4 + O(k^2)$ as $|k| \to \infty$. Hence,

$$L(k) \equiv -\frac{K(k)}{B(1 - h^2/12)(k^2 + X^2)^2} = 1 + O(k^{-2}),$$

where $X > \delta$ is an arbitrary positive constant. Since both $K(k)$ and $(k^2 + X^2)^2$ are analytic and non-zero in the strip $\mathcal{D}$, so too is $L(k)$, and hence $\log L$ may be defined so as to be analytic in $\mathcal{D}$. Using Cauchy's integral representation,

$$2\pi\mathrm{i}\log(L(k)) = \int_{-Y-\mathrm{i}\delta}^{Y-\mathrm{i}\delta} + \int_{Y-\mathrm{i}\delta}^{Y+\mathrm{i}\delta} + \int_{Y+\mathrm{i}\delta}^{-Y+\mathrm{i}\delta} + \int_{-Y+\mathrm{i}\delta}^{-Y-\mathrm{i}\delta} \frac{\log(L(\xi))}{\xi - k}\,\mathrm{d}\xi,$$

where the integration contours are straight lines between the endpoints, and k lies inside this closed contour. Since $\log(L(\xi))/(\xi - k) = O(\xi^{-3})$, the end integrals tend to zero as $Y \to \infty$ and the other two integrals converge, so that

$$\log(L(k)) = \frac{1}{2\pi\mathrm{i}} \int_{-\infty-\mathrm{i}\delta}^{\infty-\mathrm{i}\delta} \frac{\log(L(\xi))}{\xi - k}\,\mathrm{d}\xi - \frac{1}{2\pi\mathrm{i}} \int_{-\infty+\mathrm{i}\delta}^{\infty+\mathrm{i}\delta} \frac{\log(L(\xi))}{\xi - k}\,\mathrm{d}\xi. \tag{29}$$

The first integral is analytic for $\mathrm{Im}(k) > -\delta$, and similarly the second integral is analytic for $\mathrm{Im}(k) < \delta$. Calling the first integral $\log(L^+(k))$ and the second integral $\log(L^-(k))$ gives the decomposition $L(k) = L^+(k)/L^-(k)$. Hence

$$\begin{aligned} K^+(k) &= \mathrm{i}\big(B(1 - h^2/12)\big)^{1/2}\big(k + \mathrm{i}X\big)^2 L^+(k) \\ K^-(k) &= -\mathrm{i}\big(B(1 - h^2/12)\big)^{-1/2}\big(k - \mathrm{i}X\big)^{-2} L^-(k) \end{aligned}$$

gives the required decomposition $K(k) = K^+(k)/K^-(k)$. Noble (ref. 17, p. 15, theorem C) states that the L^+ and L^- found using this method remain bounded as $|k| \to \infty$ provided $\log L = O(k^{-q})$ as $|k| \to \infty$ for $q > 0$, which is certainly the case here. Hence, $K^+(k) = O(k^2)$ and $K^-(k) = O(k^{-2})$.

Requiring $K^+/K^- = K$ with K^+ and K^- analytic and non-zero in their respective half planes determines K^+ and K^- up to multiplication by an arbitrary analytic non-zero function. Since the asymptotic behaviour of these specific K^+ and K^- is known, they are in fact specified up to multiplication by an arbitrary constant. This is the degree of freedom provided by the arbitrary constant X above. However, such a constant has no effect on the final solution, as can be seen from (23).

The decomposition of $\mathrm{i}\omega Z_0(k)K^-(k)$ into $F^+(k)+F^-(k)$ is more simple. The only poles of $\mathrm{i}\omega Z_0(k)K^-(k)$ in the lower half plane are the simple poles of $\mathrm{i}\omega Z_0$ at k_l and k_t. Hence, $F^-(k) = \mathrm{i}\omega Z_0(k)K^-(k) - F^+(k)$, where

$$F^+(k) = \frac{R_l}{k - k_l} + \frac{R_t}{k - k_t}, \tag{30}$$

and R_l and R_t are the residues of $\mathrm{i}\omega Z_0(k)K^-(k)$ at k_l and k_t, given in (24). The large k behaviour of F^+ and F^- is easily derived from (19), (30), and the asymptotic behaviour of $K^-(k)$, giving $F^+(k) = O(k^{-1})$ and $F^-(k) = O(k^{-1})$ as $|k| \to \infty$.